

Mechanochemical modelling of dorsal closure reveals emergent cell behaviour and tissue morphogenesis

Francesco Atzeni^{1,2}, Laurynas Pasakarnis¹, Gabriella Mosca³, Dominika Tworus¹, Richard S. Smith⁴, Christof M. Aegerter^{1,2} and Damian Brunner¹

¹ Department of Molecular Life Sciences, University of Zurich, Winterthurerstrasse 190, 8057 Zurich, Switzerland.

² Department of Physics, University of Zurich, Winterthurerstrasse 190, 8057 Zurich, Switzerland.

³ Department of Plant and Microbial Biology, University of Zurich, Zollikerstrasse 107, 8008 Zurich, Switzerland.

⁴ Max-Planck-Institut für Pflanzenzüchtungsforschung, Carl-von-Linné-Weg 10, 50829 Köln

Running title: Modelling of dorsal closure

Abstract

Tissue morphogenesis integrates cell type-specific biochemistry and architecture, cellular force generation and mechanisms to coordinate these forces amongst neighbouring cells and tissues. Here, we use finite element-based modelling to explore the interconnections at these multiple biological scales in the developmental process of dorsal closure, where pulsed actomyosin contractility in adjacent Amnioserosa (AS) cells powers the closure of an epidermis opening. Based on *in vivo* observations, the model implements F-actin nucleation periodicity that is dependent on Arp2/3 but not MyoII activity. Our model shows how depleting MyoII activity can indirectly affect oscillatory F-actin behaviour without biochemical feedback. In addition, it questions the previously proposed role of Dpp-mediated regulation of patterned actomyosin dynamics in the AS tissue. Tissue-specific Dpp interference supports the model's prediction. The model further predicts that the mechanical properties of the surrounding epidermis tissue feed back on the shaping and patterning of the AS tissue. Finally, our model's parameter space reproduces mutant phenotypes and provides predictions for their underlying cause. Our modelling approach thus reveals several unappreciated mechanistic properties of tissue morphogenesis.

Keywords: Cell oscillations / crossing scales / dorsal closure / emergent tissue morphogenesis / finite element modelling

Introduction

The morphogenesis of tissues and organs is the result of a complex interplay of mechanical and biochemical signalling processes. These control the growth and differentiation states of individual cells in space and time and their cooperative or collective behaviour. A key task is to generate cellular forces that change cell and tissue shape. These forces need to be precisely timed and mechanically balanced in order to generate a desired morphology. In addition, developing tissues are mostly embedded in a tissue environment that itself changes shape with cells following their own morphogenetic programs, which is prone to generate mutual interference. In particular, cells at tissue-tissue boundaries need to adapt to dynamically changing biochemical and mechanical environments and cell-cell contacts. When observing changes in cell behaviour and architecture it is often difficult to separate effects caused by cell autonomous processes and effects superimposed by the environment. Similarly, it is difficult to determine which aspects of cell and tissue behaviour are regulated and which are emergent. Explorative mathematical modelling provides a powerful means to address such intertwined processes.

Dorsal closure (DC) is a relatively simple morphogenetic process occurring in *Drosophila melanogaster* embryogenesis, where modelling has been extensively used in various studies (Kiehart *et al*, 2017; Aristotelous *et al*, 2018). DC comprises the closure of a large opening in the dorsal embryonic epidermis (ES). It can be selectively manipulated and imaged live with sub-cellular resolution, which makes it particularly well suited to address the impact of cellular scale biochemistry and force generation on tissue scale morphogenesis and tissue-tissue interactions. Several force producing mechanisms were identified that occur in the two relevant tissues, the closing ES tissue and the contracting amnioserosa (AS) tissue, which fills the opening (Kiehart *et al*, 2000; Solon *et al*, 2009; Sokolow *et al*, 2012; Saias *et al*, 2015). Selective MyoII activity interference in the two tissues showed that apical constriction of the AS cells provides the critical force for convergence of the epidermis fronts (Pasakarnis *et al*, 2016). When these fronts have come close enough for the dorsal-most epidermis cells (DMEs) to engage, the latter start pulling on each other. This force drives the sequential sealing of the opening, starting at the anterior and posterior canthi from where it "zips" towards the middle of the opening.

Suppression of this zipping force reveals a maximal, autonomous contractility of the AS tissue. The underlying apical constriction process lasts for 3-4 hours and is driven by superimposed periodic apical cell surface area contractions that occur with a periodicity of 2-3 minutes (Solon *et al*, 2009). Dynamic, contractile actomyosin networks transiently forming at random positions of the apical plasma membrane produce this oscillatory behaviour (Blanchard

et al, 2010). It is not clear how these AS cell surface area oscillations begin translating into apical constriction at the onset of closure.

Coinciding with this transition is the beginning of an oscillation amplitude decrease, which continues until cells eventually arrest. This occurs in a patterned manner, with the smallest AS cells at the anterior and posterior canthi of the eye shaped opening arresting first, followed by the ventral-most cells and then sequentially, by the more centrally situated (Solon *et al*, 2009; Blanchard *et al*, 2010). A gradient of *dpp*, secreted by the dorsal-most ES cells comprising the boundary to the AS tissue (DMEs), was proposed to control apical constriction of AS cells (Lada *et al*, 2012). In addition, mechano-chemical coupling of neighbouring AS cells was suggested to provide tissue autonomous regulation (Hunter *et al*, 2014). Furthermore, genetic interference with actomyosin dynamics, suggested additional, cell autonomous regulation, where the periodic bursts of apical F-actin formation in AS cells require a feedback from contractile non-muscle myosinII (MyoII) activity (Azevedo *et al*, 2011; David *et al*, 2013; Saias *et al*, 2015).

Here, we question such a role for MyoII, as we show experimentally that oscillatory F-actin dynamics occur in the absence of MyoII activity and mechanical coupling. Based on these findings, we established a multi-scale modelling approach that, unlike previous modelling of DC, integrates biochemistry governing subcellular scale actomyosin organisation and the mechanics of MyoII-driven AS cell- and tissue shape changes (Aristotelous *et al*, 2018). We implemented our model using the finite element method (FEM), which can handle complex geometries and their deformation through discretisation into numerous, simple elements (e.g. triangles, quadrilaterals, tetrahedra). FEM-based simulations have been used to describe how complex biological structures form during development (Brodland & Clausi, 1995; Davidson *et al*, 1995). Recently, FEM was also used to simulate reaction diffusion equations coupled to material contractility on simple spherical shapes (Brinkmann *et al*, 2018). We here similarly combined tissue mechanics with cellular actomyosin biochemistry in AS cells, segmented from a living embryo, to simulate and explore AS tissue dynamics during DC.

Exploring the model's free parameter space revealed that depleting MyoII activity can indirectly affect F-actin dynamics without the need for direct feedback on F-actin biochemistry, as generally assumed. Furthermore, it predicted emergence of a previously described, graded AS cell pulsation arrest, which so far seemed controlled by a corresponding Dpp signalling gradient. Supporting the model's prediction, AS tissue-specific interference with Dpp signalling *in vivo*, showed no effect on DC. In addition, the model showed that both, the pattern with which AS cells arrest and the overall AS tissue shape changes critically depend on the mechanical properties of the surrounding epidermis tissue. Finally, several of the thousands of

solutions, provided a clear cause for some of the cell and tissue phenotypes that had been reported for genetic mutants. They thus make a specific prediction for the role of the respective proteins. Altogether, our modelling approach generates several unexpected mechanistic views on morphogenesis in general and DC in particular.

Results

Periodic F-actin dynamics are MyoII-independent

The oscillating actomyosin dynamics of AS cells were proposed to depend on MyoII activity but so far supporting experimental data have not been shown (David *et al*, 2013). We therefore tested this by selectively interfering with MyoII activity using the deGradFP system in AS cells (Caussin *et al*, 2012; Pasakarnis *et al*, 2016). These expressed the mCherry tagged F-actin-binding domain of Moesin to visualise F-actin dynamics (mCherry-moesin). As previously shown, the AS cells of such AS-SqhKO embryos completely lacked MyoII dynamics, showed no apical cell surface oscillations and could not apically constrict thus failing DC (Pasakarnis *et al*, 2016). Surprisingly, we found that F-actin dynamics were not much affected in AS-SqhKO embryos (Fig. 1A; Movie 1; Methods). Similar to the wild type, local F-actin foci formed in all cells and migrated across the apical cell surfaces similar to the wild type, before vanishing again. Generally, the appearing F-actin foci had reduced signal intensity. However, this is expected, as due to the lack of MyoII activity these foci will not contract. In the wild type contraction concentrates the actin filaments, which locally strongly enhances the detectable signal. Compared to the wild type, the periodicity of F-actin foci formation was only slightly longer (Fig. 1B). This result contrasts a previous study mentioning the absence of periodic F-actin nucleation in embryos that were homozygous mutant for *zipper* (*zip^l*), the gene encoding MyoII heavy chain (David *et al*, 2013). However, when imaging *zip^l* embryos expressing mCherry-moesin, we found periodic F-actin dynamics very similar to those in AS-SqhKO embryos (Fig. 1C). These data show that the periodically forming F-actin networks of AS cells are not dependent on MyoII activity.

The periodically forming F-actin foci looked very much like a branched F-actin network as is typically nucleated by the Arp2/3 protein complex (Rotty *et al*, 2012). To test for a role of Arp2/3 in AS cells we injected CK-666, a drug that selectively inhibits Arp2/3, into mCherry-moesin expressing AS-SqhKO embryos at an early DC stage (stage 13). The drug was released into the yolk cell below the AS tissue (Materials and Methods) (Hetrick *et al*, 2013). This suppressed the formation of the MyoII-independent F-Actin foci in the AS tissue indicating that Arp2/3 provides the relevant F-actin nucleating activity (Fig. 1D, Movie 2). Suppression was transient as presumably the drug diluted out over time.

Close examination of AS cells expressing mCherry-moesin in otherwise wild type embryos revealed the presence of a loose, stable F-actin network that covers the entire cell apex (Fig. 1E). The network globally deforms in response to the localised, periodic actomyosin contractions but seems to be connected to the peripheral regions where the adherens junctions reside. It is possible that this network provides a basic grid on which the periodic F-actin foci are seeded.

FE modelling of F-Actin dynamics in AS cells

A crucial question to address is how the relatively slow apical constriction connects to the much faster oscillating actomyosin contractility. To date, experimental limitations have hampered an unambiguous answer. For this reason, we decided to develop a computer-based, mathematical modelling approach that would allow building a tissue system to explore the mechanistic link between actomyosin activity, cellular force production, force transduction and tissue morphogenesis. For this, we combined biochemical reactions relevant to cytoskeleton dynamics with cell and tissue mechanics in a FEM-based implementation of the DC process. In our custom program, we implemented an image-based discretisation of roughly 150 cells comprising a typical AS tissue. The surrounding ES tissue was similarly discretised, but without subdividing it into cells (Fig. 2A). As a basis, we generated a region that was entirely subdivided into linear hyper-elastic triangular elements on which the mechanical problem was solved using the finite element method (Appendix Supplementary Methods). The region was further subdivided such that an outer ring of "mechanical elements" constituted the ES tissue while the central area was subdivided into cells constituting the AS tissue. The mechanical elements of each AS cell were further subdivided, to generate a finer "biochemical" mesh, onto which we implemented the actomyosin activity (Fig. 2A). Actomyosin modelling was exclusively performed in the AS tissue, while the contribution of the surrounding ES tissue was purely mechanical and thus passive. We modelled apical cell surfaces only, where the relevant actomyosin dynamics and force transmission are known to take place (Martin & Goldstein, 2014). The biochemistry was implemented with a reaction-diffusion equation-based model that produced the periodic formation of F-actin foci in a spatially resolved manner (Appendix Supplementary Methods). Diffusion of the components was restricted by cell boundaries. Based on our *in vivo* experiments, we designed a model for oscillating F-actin formation dynamics that is dependent on Arp2/3 but independent of MyoII. We simplified by integrating Arp2/3 and its regulatory proteins into a species we term Actin Nucleating Proteins (ANPs). These are produced in an inactive state (ANPi) and can become activated (ANPa) (Fig. 2B). To model spontaneous, local triggering of ANP activation, we use a Turing patterning mechanism (Turing, 1952) (Appendix Supplementary Methods). The reactions were built on the activator-

depleted substrate model from Gierer and Meinhardt, 1972 (Gierer & Meinhardt, 1972). These ANP dynamics were then coupled to an additional species that modelled F-actin.

Our model comprised the following interactions, the equations of which we provide in the Appendix Supplementary Methods: ANPi is produced at a constant rate and is activated to become ANPa at a rate that depends on ANPi and ANPa concentration (Fig. 2B). ANPa leads to F-actin formation at a linear rate. Similarly, ANPa depletion and F-actin disassembly occur at a linear rate. Furthermore, we assume negative Hill-type F-actin feedback on ANP activation. This introduces the previously reported negative feedback of F-Actin on the activity of Rho-GTPases (Bement *et al*, 2015; Robin *et al*, 2016; Segal *et al*, 2018). Notably, in our simulations we found this feedback to increase the number of parameter combinations that produce oscillatory dynamics suggesting that this feedback merely serves to provide additional robustness (Appendix Supplementary Methods). Consistent with the original Gierer-Meinhardt model, we implement a negative Hill-type feedback on ANP activation, which eventually leads to a saturation of ANPa production. ANPa concentration cannot drop below a minimal level, which not only improved the stability of computer simulations but also provided a parameter, the modulation of which allowed simulating certain mutant *in vivo* scenarios (see below).

Having found that actin bursts and waves were present in the absence of MyoII *in vivo*, we first explored the parameter space of our reaction-diffusion model to identify the conditions that qualitatively reproduced a similar oscillatory F-actin behaviour. To home in on the greater area of the parameter space of interest, we first fixed the parameters of the reaction part of the equations using standard dynamical systems theory (Murray, 2004). Next, we fixed the ANP diffusion coefficients. For the ANPi diffusion coefficient, several publications suggest that $10\mu\text{m}^2/\text{s}$ is a reasonable value (Mogilner & Edelstein-Keshet, 2002; Holmes *et al*, 2012). The ANPa diffusion coefficient should be considerably lower, as much of the ANPa will be F-actin bound. Lacking sufficient relevant experimental information, we again used theoretical methods to calculate the range of ANPa diffusion coefficients that would lead to oscillatory F-actin dynamics as observed *in vivo* (Appendix Supplementary Methods).

We applied this system of reaction-diffusion equations to the tissue geometry that we had extracted from an image of a living embryo (Fig. 2A). For this, we chose the time point of DC when the two lateral ES tissue fronts had just made their initial contact at the anterior end of the opening to fully enclose the AS tissue. Simulations were initialised with starting concentrations of ANPi, ANPa and F-actin set to zero (Fig. 2C). To quantify the subcellular spatial pattern of F-actin over time, we extracted the cell area fraction that was covered by F-actin at each time point: Below 20% coverage we considered a cell to be passive, above

60% coverage to be globally active and in between to be locally active (Appendix Supplementary Methods). Initially, all cells simultaneously increased their ANPi, and consequently their ANPa and F-actin concentration, causing synchrony of the first F-actin oscillation cycle (Fig. 2D). Cells gradually de-synchronised in the following cycles until oscillations reached an equilibrium distribution (Fig. 2D; Movie 3). Thereby, cells alternated between passive and locally or globally active states over time (Fig. 2C). Once the initial synchrony of activation was broken, the average fraction of cells in each of the categories converged to a stable value at any given time point (Fig. 2D). To explore the dependence of this equilibrium value on the chosen parameters, we systematically changed the production rates of ANPi and ANPa (Fig. 2E). The resulting 2-dimensional parameter spaces showed that for low values of both parameters most cells were passive. The other cells had high oscillation amplitudes and periods. As the ANPi production rate increased, the number of passive cells gradually decreased, while the number of cells with F-actin oscillations increased (Fig. 2E). Concomitantly, these cells showed decreasing periodicity and amplitudes. In summary, our conceptualisation of a basic F-actin biochemistry, for defined parameter values, is able to produce oscillatory F-actin dynamics that resemble the dynamics observed *in vivo*, in wild type and MyoII mutant AS cells.

MyoII forces modulate oscillatory F-actin dynamics

After our modelling system reproduced F-actin oscillations, we went on to explore how these oscillations react to MyoII force action, by connecting the biochemical and mechanical finite element models (Fig. 2A). Since oscillatory F-actin dynamics occur independent of MyoII activity, there is in principle no need for additional MyoII regulation. Therefore, we assumed that the motor protein by default binds to F-actin and is present in an active form at non-limiting concentration. In this scenario, the oscillating F-actin concentration is the critical variable controlling contractility (Fig. 3A). In addition, we assumed that we need a critical amount of F-actin bound MyoII, in order to produce a force that is sufficient to initiate contraction. Such a relationship between F-actin and contractility can be described with a Hill function, whereby contractility sharply increases until a maximal value (c_{Max}) once F-actin concentration is above a threshold concentration (c_{Fthr}) (Appendix Supplementary Methods). In our finite element implementation this means that the overall F-actin concentration of all biochemical finite elements within a mechanical finite element governs its contractility. Notably, the degree of contraction of a mechanical element in addition is governed by the elastic material properties and the contractility of the surrounding elements (Appendix Supplementary Methods). We assumed that any cell surface area changes introduced by MyoII activity will not affect the amount of ANPi production, which remained constant throughout the closure process. *In vivo*,

this would reflect that the amount of Arp2/3 complex reaching the apical cell surface is constant, independent of surface size.

We first ran simulations implementing the ES tissue surrounding the AS tissue as a linear elastic material. In this way, the ES tissue provided resistance to the closure forces generated by the AS cells. In our model, changes of F-actin concentration instantaneously translated into contractility changes, such that cellular F-actin concentration peaks and cell area minima occurred simultaneously, and *vice versa* (Fig. 3B). Again, cellular F-actin oscillations started synchronously but rapidly converged towards a non-synchronous equilibrium (Fig. 3C, Movie 4). Interestingly, for a given set of reaction diffusion equation parameters, the added contractility changed the equilibrium features. In particular, we found that certain combinations of ANPi and ANPa production rates produced oscillating F-actin activity only after contractility was added (Fig. 3D). Hence, our model predicts that also *in vivo*, conditions can exist under which MyoII activity becomes essential for periodic F-actin nucleation even in the complete absence of any biochemical feedback (Fig. 2E and 3D).

As in the simulations lacking contractility, increasing ANPi and ANPa production rates in the presence of contractility decreased the average relative amplitude and the average period of oscillations, albeit not to a similar extent (Fig. 2E and 3D). In contrast however, the added contractility influenced the fraction of cells with local or global F-actin activity. For ANPi and ANPa production rates larger than those included in Fig. 3D, less and less cells were passive, and gradually, all of them became globally active. While it seems trivial that with increasing ANPi and ANPa production rates, also the frequency of F-actin structures in cells increases, it is less obvious that this results in oscillations with smaller amplitudes. Notably, this again shows how MyoII activity can indirectly modulate cellular F-actin behaviour without direct biochemical feedback.

The emergent influence of MyoII activity on F-actin dynamics made us address how the latter depends on the key parameters determining contractility, c_{Max} and c_{Fthr} . Increasing c_{Max} , which represents increasing MyoII activity, progressively decreased the fraction of passive cells, independent of c_{Fthr} (Fig. 3E). This is caused by a combination of two effects: First, the contraction process locally increased the F-actin concentration and second, F-actin structures became more persistent, with the reaction diffusion equation parameters modulating this latter effect. Furthermore, we found that with increasing c_{Max} , also the average oscillation period increased, at least for relatively high values of c_{Fthr} . This indicates that the effect of persistent F-actin structures dominates the contraction-mediated effect. Notably, the lowest tested values of c_{Fthr} biologically do not make much sense as they would correspond to MyoII-driven contractility at low F-actin concentration. As c_{Fthr} was increased from such low values to higher values, the average amplitude of oscillations

rapidly increased, while the fraction of passive cells decreased (Fig. 3E). This occurs because high cF_{thr} corresponds to MyoII-binding only taking place in regions with sufficiently high F-actin concentrations, which results in strong local contractions that can deform neighbouring cells. This scenario reflects the *in vivo* behaviour of AS cells (Solon *et al*, 2009; Blanchard *et al*, 2010).

Perturbing actomyosin dynamics in simulations, enabled us to address the coordination of actomyosin dynamics between neighbouring cells. Experimental investigation had shown that neighbouring cell areas mainly oscillate either in anti-phase or in-phase, with a preference for the former (Solon *et al*, 2009). Later, the orientation of neighbouring cells was suggested to determine the preferred mode of coordination, causing stripes of cells to contract in phase (Blanchard *et al*, 2010). In our modelled system, the sub-cellular actomyosin dynamics of a given cell and the resulting contractility, influence the actomyosin dynamics of neighbouring cells by changing their geometry independent of chemical cell-cell coupling. We wondered whether such mechanical coupling between cells would lead to any preferred phase shift between neighbouring cells. To quantify such phase shifts, we used the amount of F-actin close to the junction between the two cells as a proxy for contractility (Appendix Supplementary Methods). In-phase oscillations corresponded to F-actin concentration peaking at the same time in neighbouring cells, while anti-phase oscillations corresponded to a peak occurring in one cell while the neighbour was in a valley. Varying the production rates of ANPi and ANPa in simulations with MyoII activity, revealed a prevalence of in-phase oscillations in correlation with higher amplitudes (Fig. 3D). However, if contracting regions covered larger subcellular areas, we observed a tendency towards anti-phase oscillations (Fig. 3D). In contrast, varying $cMax$ and cF_{thr} did not produce any clear trends neither concerning oscillation amplitudes and period nor fraction of passive and locally active cells (Fig. 3E). In summary, we find that variation of few parameters in our system generated a wide variation of oscillation coordination patterns between neighbouring cells, simply due to added contractility and without the need for biochemical coupling.

ES tissue relaxation provides DC progression and emergent AS cell pulsation arrest

The previous simulations treat the ES tissue as a passive, elastic material that provides increasing resistance to the closure forces generated by the AS cells. Consequently, an equilibrium resulted, which rather quickly halted closure. *In vivo* however, several rows of ES cells at the AS tissue boundary elongate significantly along their dorsal-ventral axis, suggesting that the ES tissue relaxes during DC (Riesgo-Escovar & Hafen, 1997). To explore this possibility we implemented gradual ES tissue relaxation in our simulations. Since a time-resolved, rheological characterization of ES cells is missing, we assumed simple Maxwell-like

relaxation at a constant relaxation rate (Appendix Supplementary Methods). The relaxation timescales used in this work were chosen such that simulated and *in vivo* closure progressed similarly. These were in the order of tens of minutes, which is only slightly larger than what was experimentally measured in other comparable systems (Étienne *et al*, 2015; Doubrovinski *et al*, 2017; Atzeni *et al*, 2019). We further assumed that relaxation is isotropic everywhere in the ES tissue, except along the anterior-posterior axis (Fig. 4A). The latter accounts for the fact that *in vivo* the AS tissue does not shorten in the anterior-posterior direction during DC (Harden *et al*, 2002). Before activating relaxation, we ran each simulation without relaxation for a time period bringing the system close to the oscillations equilibrium (see previous section). This scenario is realistic as *in vivo*, the AS cells oscillate around a constant opening area prior to the onset of ES cell elongation and tissue convergence (Blanchard *et al*, 2010).

Implementing relaxation was sufficient to provide closure progression. In the simulations, the opening area first decreased slightly before stabilising around an equilibrium given by the ES tissue elasticity. When relaxation started the opening area continued decreasing with a rate that was not only set by the ES tissue relaxation rate, but also by the parameters of the reaction-diffusion equations (Fig. 4B, Movie 5). If the relaxation timescale was sufficiently fast, we observed that cell pulsing eventually arrested coinciding with the cessation of F-actin oscillations (Fig. 4C). Thereby, cells transitioned from the dynamic spatial F-actin organisation distribution at the initial equilibrium to a uniform, high F-actin concentration covering their entire surfaces (Fig. 4D, Movie 5). Interestingly, this emergent F-actin oscillation arrest was temporally and spatially patterned: the first cells to reach complete F-actin coverage were generally directly at or very close to the tissue boundary. From there, the behaviour progressed through the tissue towards the middle of the opening as if following a gradient. Intriguingly, a similar sequential pulsation arrest of AS cells had been observed to occur *in vivo*, where it was associated with the maintenance of tissue tension (Solon *et al*, 2009). In our simulations, the consequence of this sequential pulsation arrest was a slowing down of overall AS tissue constriction until closure eventually came to a halt when reaching the maximal effect of contractility. This phenocopies the closure behaviour of embryos in which the force contribution of the zipping process was suppressed (Jankovics & Brunner, 2006).

Dpp signalling interference in AS tissue does not affect DC

Our simulations predict that graded AS cell pulsation arrest is an emergent property of the system. *In vivo* however, it seemed plausible that such behaviour was controlled by a gradient of the Dpp signalling protein that is known to be secreted at the onset of DC by the

DME cells experiencing Jnk signalling (Riesgo-Escovar & Hafen, 1997). Consistently, zygotic mutants of the Dpp receptor thickveins (*tkv*), amongst other defects, were shown to interfere with AS cell apical constriction but not apical cell surface oscillations (Fernández *et al*, 2007). This was linked to Dpp's role in contributing to the expression of the MyoII heavy chain component zipper (*zip*) in AS cells (Zahedi *et al*, 2008). A Dpp signalling-mediated gradient of MyoII protein levels and activity could well account for the sequential arrest of AS cell surface oscillations. To investigate the discrepancy between simulations and *in vivo* experiments, we turned to *in vivo* experimentation. We first monitored DC in embryos expressing GFP, equipped with a nuclear localisation sequence, under the control of a *dad* enhancer element (*dad*-GFP^{NLS}) that selectively responds to Dpp signalling activity (Ninov *et al*, 2010). In wild type embryos, *dad*-GFP^{NLS} revealed a clear Dpp signalling activity gradient across the AS tissue that persisted throughout DC (Fig. 4E; Movie 6). A differential Dpp response already became visible in AS cells with the beginning of germ band retraction, which contradicts previous findings suggesting a first round of Dpp exposure occurring shortly after germ band extension (Movie 6) (Garcia Fernandez *et al*, 2007). Well established is the Dpp signalling event induced by JNK activity in the DMEs at the onset of DC (Riesgo-Escovar & Hafen, 1997; Fernández *et al*, 2007). This second Dpp activity became visible following a short period of constant *dad*-GFP^{NLS} signal intensity. It had limited effect on the AS tissue as only the AS cells closest to the DMEs further increased their nuclear GFP signal in the following hours (Movie 6). In contrast, the nuclear GFP signal in multiple rows of the surrounding ES cells started gradually increasing with DC onset, eventually becoming very bright towards the end of the process. This suggests that a graded response of AS cells to Dpp signalling is established prior to DC, at around the onset of germ band retraction and that the second Dpp signalling activity during DC mainly targets the cells of the ES tissue. Furthermore, it indicates continued Dpp signalling by DMEs throughout DC.

Potentially, the graded exposure of AS cells to the first Dpp signalling event could still determine the apical constriction behaviour of AS cells later on. A problem with previous studies interfering with Dpp signalling was that they used zygotic mutants or global RNAi interference to perturb Dpp activity. Interference thus lacked temporal control and tissue specificity, which hampers the unambiguous interpretation of the resulting phenotypes. To circumvent this problem and specifically explore the requirement of Dpp in AS cells, we selectively interfered with Dpp signalling in the AS tissue (Materials and Methods). First, we ectopically expressed a constitutively active form of the Dpp receptor thickveins (*Tkv*^{Act}) in the AS tissue of embryos expressing *dad*-GFP to monitor Dpp signalling activity. This gradually enhanced *dad*-GFP expression in AS cells during DC, such that also cells in the tissue centre showed a strong nuclear GFP signal (Fig. 4E). Despite the increased Dpp signalling in AS cells,

DC proceeded normally. Next, we suppressed Dpp signalling by overexpressing Dad, an inhibitor of the Dpp signalling response in the AS tissue (Tsuneizumi K., Nakayama T., Kamoshida Y., Kornberg T.B., Christian J.L., Tabata T. (1997) Daughters against Dpp modulates Dpp organizing activity in Drosophila wing development Nature 389:627-31). This almost completely abolished Dpp signalling response in the AS tissue but again did not affect DC (Fig. 4E). Together these results suggest that Dpp signalling does not critically affect AS tissue behaviour.

AS and ES tissue properties determine tissue patterning and shaping

Having found good evidence that differential AS cell behaviour is an emergent property of the system, we investigated which parameters and assumptions in our model were critical for the sequential arrest of cell surface oscillations. We defined the time of pulsation arrest as the last time step in which the cell is not fully covered by F-actin. We assumed that ES tissue relaxation and thus DC begins after 80min of simulation time and set a relaxation time constant of 10min to allow closure to proceed within a reasonable computational time (Fig. 4B). Simulations were run for a maximum of a day of computational time or 250 minutes of simulation time. First, we varied the contractility parameters, as before when exploring the role of MyoII. When cF_{thr} was high and $cMax$ low, cell areas oscillated but only very few AS cells showed pulsation arrest (Fig. 5A). The number of arresting cells increased if simulations were run for longer or if faster ES tissue relaxation was implemented (Appendix Supplementary Methods). This occurred also if $cMax$ was increased, for any given value of cF_{thr} . In this scenario, cells arrested sequentially, starting from the outside towards the middle of the opening. Interestingly, if $cMax$ increased further at low cF_{thr} values, some cells stopped oscillating even before the beginning of ES tissue relaxation. When both cF_{thr} and $cMax$ were high, the cell's oscillation amplitudes were much increased and passive phases were extended (Fig. 3E). This caused faster AS tissue contraction, while area differences between cells were also larger and shorter lived. At the same time, pulsation arrest was more synchronous.

Next, we tested whether and how ANPi and ANPa production rates affected the patterned arrest of AS cell pulsing. To facilitate this analysis, we sped up simulated closure progression by fixing $cMax = 2$ and $cF_{thr} = 1.5$. Under these conditions, the sequential nature of pulsation arrest turned out to be remarkably robust towards changes in ANPi and ANPa production rates (Fig. 5B). Obviously, oscillation arrest could only be monitored for parameter combinations that did lead to oscillations in first place, such as low ANPi production. In this case, the opening in addition did not contract. Similarly, high ANPi production rates caused absence of oscillations, but for another reason: Many cells arrested oscillating before ES

tissue relaxation began. In contrast to cases with low ANPi production, this situation produced a strong tissue contraction,

Finally, we explored to what extent the mechanical properties of the ES tissue would affect the oscillatory behaviour and the pattern of contractility arrest of AS cells. Therefore, we fixed the actomyosin and mechanical parameters defining the AS tissue and selectively varied the resistance of the elastic ES tissue by modulating its geometry and its material parameters. First, we reduced the initial resistance by simply enlarging the simulated ES tissue (Figure 5C-D, Movies 7 and 8). As expected, this caused increased AS-shrinkage already before relaxation began (Fig. 5C, first two time points). If enlargement and thus resistance reduction was only implemented along one axis, the AS tissue shrank faster along this axis which altered AS tissue shape accordingly (Fig. 5C-D). Notably, not only the shape of the closing AS tissue varied, but also the pattern of sequential AS cell pulsation arrest (Fig. 5C-D, third and fourth timepoints). To further explore this effect of the epidermis tissue on AS cell actomyosin dynamics we systematically varied the ES tissue width along the DV-axis and the Young's modulus of the ES tissue (Fig. 5E). So far, we had been using an ES tissue stiffness of $E=1\text{kPa}$. If the tissue was stiffened by increasing E , closure eventually could not proceed far enough for pulsation arrest to occur. Conversely, if the tissue was softened by increasing its width, closure eventually proceeded so fast that cells became fully covered by F-actin without ever oscillating. When the tissue was simultaneously hardened and enlarged, cells at the tissue boundary oscillated again and regained sequential arrest. Not surprisingly for a linear material, the effects of stiffness and width equilibrated. Intriguingly however, in case of low values for E and width, the direction of pulsation arrest progression turned by 90 degrees within the tissue as compared to the pattern emerging with high values for stiffness and width. Taken together, these data show that the mechanical properties of the ES tissue fundamentally influence the AS tissue shape and its patterning with respect to the oscillatory behaviour of individual AS cells in space and over time.

To estimate the extent to which our results were specific to the particular *in vivo* geometry we had selected, we repeated critical simulations on artificial geometries, where all AS cells were regularly arranged and identical in shape. We found the same effects on AS tissue shape and patterning but with the resulting patterns being much more regular than with the *in vivo* geometries (Fig 5F; Appendix Supplementary Methods).

Simulations reproduce *in vivo* mutant AS cell behaviour

Starting from a scenario best reflecting wild type AS cell dynamics (Fig. 2D, Movie 4, Fig. 6B), and then varying the model parameters, our simulations produced a range of interesting cellular behaviours. We therefore checked if any of these simulations would reproduce mutant

phenotypes as observed *in vivo*. *In vivo*, MyoII activity levels in AS cells have been manipulated by genetic interference or by interference with the MyoII phosphorylation levels either via ectopic expression of the inhibiting MyoII phosphatase (MbsN300) or the activating MyoII light chain kinase (ctMLCK) (Franke *et al*, 2005; Fischer *et al*, 2014; Saias *et al*, 2015). MbsN300 expression produced larger AS cells and tissue softening. Subsequently, a highly irregular pattern of apical AS cell constriction emerged. Conversely, ectopic ctMLCK expression produced smaller AS cells with longer-lasting contractile events and higher tissue tension. In our simulations, varying the threshold F-actin activity for contractility (cFthr) and the maximal contractility (cMax) mimicked loss and gain of MyoII activity. Activity gain correlated with increased cMax and decreased cFthr. This produced a phenotype very similar to that of ectopic ctMLCK expression: AS cells were smaller and exhibited longer-lasting and stronger contractile events (Fig. 6C, Movie 9). To mimic MyoII loss of activity, we reduced cMax. This produced a phenotype similar to that of ectopic MbsN300 expression, leading to AS cells that hardly contracted (Fig. 6D, Movie 10). This phenotype resembled another *in vivo* mutant phenotype that was observed in embryos maternally mutant for *rhoGEF2*, encoding the *Drosophila* Guanine nucleotide exchange factor of Rho GTPases (Azevedo *et al*, 2011). In these mutants, actomyosin coalescence significantly decreased and hardly any contraction occurred. Our simulations also phenocopied these effects. This is fully consistent with the suggested role of RhoGEF2 in promoting the association of MyoII with F-actin (Padash Barmchi *et al*, 2005). In turn, RhoGEF2 over-expression *in vivo* caused increased actomyosin coalescence in AS cells and led to contractile events that lasted longer and occupied larger subcellular regions, when compared both to wild type and to ctMLCK expression. Our simulations showed similar behaviour when we mimicked RhoGEF2 overexpression by increasing cMax (Fig. 6E, Movie 11). Thus, they also provide an interpretation for the DRhoGEF2 over-expression phenotypes indicating that increased MyoII recruitment is sufficient to reproduce the phenotype.

In summary, our simulations indicate that varying actomyosin parameters at the subcellular scale is sufficient for the emergence of mutant phenotypes observed *in vivo* and they thus provide a clear interpretation.

Discussion

Our FE modelling approach enabled a systematic multiscale exploration of the mechanism integrating repetitive apical AS cell surface constrictions occurring in the minutes range with simultaneous gradual apical constriction occurring over a time period of 3-4 hours to drive DC. The approach combines basic sub-cellular biochemistry with mechanical cell- and tissue behaviour. Our simple model predicts a range of known behaviours to be emergent rather than regulated. Biochemistry modelling is based on our experimental results, showing that F-actin oscillations are similar in presence and absence of MyoII activity. This differs from the mechanisms proposed for other tissue morphogenesis processes employing oscillating cells for morphogenesis, such as the extending germ band (Munjal *et al*, 2015). There, mutant analysis suggested that oscillatory actomyosin dynamics depend on positive and negative biochemical feedback between MyoII advection and dissociation rates. Our model provides an alternative interpretation to consider, showing that under certain F-actin nucleation conditions, MyoII activity can generate oscillatory F-actin dynamics without the need for biochemical feedback. Thereby, the contractility state of a given cell, indirectly influences the F-actin dynamics of neighbouring cells by changing their geometry. In other words, dynamic geometry can substitute biochemical signalling. In view of the predictions of our model, it would be interesting to see if during germ band extension, the absence of oscillatory dynamics in cells lacking MyoII activity can be compensated by altering F-actin production rates.

Currently our model is lacking the actomyosin ring that *in vivo* starts forming at the AS cell-cell junctions following DC onset and that becomes increasingly prominent as DC progresses (Blanchard *et al*, 2010). In germ band extension, the non-uniform distribution of this actomyosin pool guides directional contractility (Rauzi *et al*, 2010). Its uniform distribution in AS cells could serve as a clutch that together with the medial-apical actomyosin pool generates a ratchet system or simply provide an additional, additive force. Arguing against the former, our model reproduces all *in vivo* behaviours found at the sub-cellular, cellular and tissue scale without this actomyosin pool. Even more, our model reproduces much of the mutant phenotypes observed *in vivo* by simply varying the parameters reflecting the affected biochemical *in vivo* activity. Thereby, the model not only shows sufficiency but suggests causative mechanisms for phenotype development, defining a mechano-chemical parameter space within which the cells need to reside for a given phenotype to occur. For example, previous *in vivo* modulation of MyoII activity produced phenotypes that could not be explained in a simple way and were hypothesised to be caused by pleiotropic effects of MyoII activity on cellular function (Fischer *et al*, 2014). Our model reproduces these phenotypes without addition of further complexity. Of course, the predictions of the model now ask for more comprehensive analysis of the *in vivo* systems. To address the contributions of the junctional and the medial-apical actomyosin pools

and their mechanical and chemical parameters to DC *in vivo*, will require spatially and temporally controlled, acute protein interference as well as careful biophysical measurements for example of tissue stiffness over time. Such analysis may well lead to a reinterpretation of some of the cellular phenotypes and the associated closure defects.

Currently, the initial event triggering DC is not known. Regulation of the pulsed contractile forces of AS cells can be excluded, as this critical activity starts prior to dorsal closure initiation. Some other change thus must occur in the AS or the surrounding ES tissue. In our model, a gradual relaxation of the ES tissue was sufficient to allow DC initiation and propagation. Such a scenario was previously proposed based on the observation that during the process the ES cells gradually elongated in the direction of tissue closure (Riesgo-Escovar & Hafen, 1997). Such tissue relaxation is generally presumed to be a fundamental mechanism of embryonic tissue morphogenesis and wound healing (Razzell *et al*, 2014; Bambardekar *et al*, 2015; West *et al*, 2017). Consistently, DC arrests if ES cell elongation is prevented by prohibiting Dpp secretion from the DME cells or by mutating the Rho/Rac effector target Pkn (Riesgo-Escovar & Hafen, 1997; Lu & Settleman, 1999). The importance of this mechanism was questioned as the selective rescue of global Dpp interference implied that Dpp signalling in addition regulates AS cell constriction, which may well be the critical activity triggering DC (Garcia Fernandez *et al*, 2007; Zahedi *et al*, 2008). However, our direct, AS tissue-specific interference with Dpp signalling, contradicts these findings, bringing Dpp-mediated ES tissue relaxation as DC initiator back into focus.

This finding in addition supports a further prediction of our simulations, namely that the sequential arrest of AS cell pulsation described *in vivo*, is not brought about by a Dpp gradient emanating from the DMEs, but simply is an emergent property of the tissue systems mechanics (Solon *et al*, 2009; Blanchard *et al*, 2010). Our simulations could reproduce the *in vivo* pattern of pulsation arrest with AS cells at the ES/AS tissue boundary arresting first and cells in the tissue centre last. Thereby, AS cells arrested in a contracted state, with their entire surface covered by F-Actin as previously described (Blanchard *et al*, 2010; Jayasinghe *et al*, 2013; Machado *et al*, 2015). *In vivo*, this effect was assigned to differential biochemical regulation over time of one or more factors of the actomyosin system. In our model, the behaviour emerges without any specific regulation. The shrinking AS cells eventually reached sufficient ANPa-levels for F-actin structures to cover their entire surfaces. This effect relied on our assumption that the amount of ANPi remains constant as the cell surface area gradually shrinks. *In vivo*, this would mean that the amount of ANPi reaching the apical plasma membrane is constant over time, a reasonable scenario, assuming directed transport. It is plausible, that the sequential nature of this effect in our simulations starts emerging at DC onset, due to the outermost AS cells on one side being connected to passive ES cells.

This means that after each contraction event, these boundary cells have fewer actively contracting neighbours than AS cells inside the tissue that drive their subsequent expansion. Consequently, they reach a fully contracted state much earlier. This effect propagates as in the contracted state the boundary cells in turn have become passive and no longer contribute to the stretching of the next inner AS cells. This generates a new, mechanical boundary that similarly accelerates pulsation arrest of the next inner AS cells. In this way pulsation arrest propagates further into the tissue over time.

Previously, we had discussed that this arrest in a contracted state could be compensating the surface tension-loss of the shrinking tissue (Solon *et al*, 2009). This is consistent with a subsequently proposed mechanism, where contracting cells stretch neighbouring cells to open mechanically gated ion channels, which induces these cells to contract in turn (Hunter *et al*, 2014). However, we show that F-actin oscillation dynamics are not affected in tissues lacking mechanical input due to MyoII activity depletion. The reported Ion channels must be serving some other important function. This is consistent with another issue addressed with our computational modelling of DC - the coordination of neighbouring AS cell surface oscillations. Quantification of experimental data indicated that neighbouring cells generally oscillate in anti-phase (Solon *et al*, 2009), or form rows of cells that contract at the same time (Blanchard *et al*, 2010). In our simulations various coordination patterns emerged depending on the biochemical and mechanical parameters in the complete absence of any biochemical coupling between neighbouring cells.

Intriguingly, in a given AS tissue with a fixed set of biochemical and mechanical parameters the pattern of the sequential pulsation arrest can differ fundamentally, solely depending on the local elastic properties of the surrounding ES tissue. Simultaneously, these properties define AS tissue shape. It is thus possible that also *in vivo* changing mechanics of surrounding tissues critically affect the patterning and morphogenesis of a tissue without it changing its molecular state. Hence, when exploring tissue and organ morphogenesis one cannot avoid considering cooperative effects of simultaneously developing tissues. This point is interesting also from an evolutionary perspective suggesting that morphological changes of a tissue are not necessarily driven by tissue-autonomous changes in gene expression.

Altogether, our simple model predicts a range of known behaviours to be emergent, which indicates the predictive power of our simulations. Importantly, these predictions emphasise the importance of identifying *in vivo* the contribution of geometry and of cell- and tissue scale mechanics to sub-cellular biochemical dynamics such as F-actin pattern modulation. In principle, our model can be adjusted to simulate other oscillatory tissues undergoing morphogenesis. It would for example be interesting to explore whether and to what extent it

could reproduce gastrulation and germ band extension, the other classical morphogenetic processes that have been intensively studied in flies.

While our results show the immense potential of FE-based modelling in enabling more complex computational exploration of living systems, they also stress the need for a holistic analysis at single cell and tissue scales of entire tissue communities for a more profound understanding of morphogenesis.

Materials and Methods

Fly strains

Fly strains used in this study are listed in Supplementary Table 1.

For AS tissue-specific interference with Dpp signalling, 332.3Gal4 (Wodarz *et al*, 1995) was used to drive tkv^{act} expression and P0172Gal4 was used to drive UAS-Dad (Tsuneizumi *et al*, 1997). Notably, expressing UAS-Dad via the 7KGal4, KrüppelGal4 (Castelli-Gair *et al*, 1994) or the combined dpp[4B] and dpp[8B]Gal4 drivers, also did not affect DC. This was not due to a lack of functionality as this combination caused adult fly lethality (data not shown).

Confocal microscopy and image processing

Embryos were prepared for imaging as previously described (Jankovics & Brunner, 2006). Imaging of all embryos was performed at 23-25°C using spinning-disk confocal microscopes (Zeiss Axio Observer.Z1 or custom-modified Leica DM IRBE, equipped with iXon3/888 and Neo sCMOS cameras and controlled by ANDOR IQ software or VisiScope Confocal-FRAP Cell Explorer). Objectives used: 25X (for dorsal closure overview), 40X, 63X and 100X. Z-planes were acquired every 2µm and maximum-intensity z projections were analysed. For higher resolution of LE cells, amnioserosa cell and MyosinII dynamics (63X and 100X objectives) z-planes were acquired every 0.5-1µm, and single planes or maximum-intensity z projections of relevant planes were analysed.

Image processing and maximum intensity z-projections were done using ImageJ or MATLAB (MathWorks).

F-actin dynamics analysis

F-actin dynamics were quantified using maximum intensity z-projections of wild type and AS-SqhKO movies of AS tissue. Using ImageJ, we first measured mCherry-moesin

fluorescence intensities in ROIs within AS cells every 30s throughout the movie sequences. The intensity oscillations were then “detrended” by subtracting the mean intensity value individually for every intensity profile. To determine the periodicity of F-actin nucleation bursts, we divided the movie frames into time windows of 900s that were shifted by 30s. For every 900s window from intensity profile auto-correlation was performed on the intensity profile (autocorr function in MATLAB). The average distance between the peaks in the auto-correlation function was taken as a period for that time window. Peaks were found using the “findpeaks” function in MATLAB without any threshold for peak heights. We then plotted period distributions according to their relative frequency (Fig. 1B).

Wild type: n=13508 CCFs, 155 unique cell pairs (= 310 cells), 3 embryos; AS-SqhKO: n=22712 CCFs, 205 unique cell pairs, 5 embryos

Drug injections

For CK-666 injections stage 12 AS-SqhKO embryos with tissue-specific MyoII activity depletion as described in Pasakarnis *et al*, 2016, were collected and processed for injection as follows: Embryos were dechorionated desiccated for 15- 25 min in the air before being aligned on a coverslip and covered with Halocarbon oil. Injections were carried out on the embryos that had meanwhile reached early stage 13, using a Zeiss Axiovert X35 upright microscope equipped with a Narishige MO-11 injection manipulator (Narishige Scientific Instrument lab, Japan). Image acquisition started within 2 to 5 min after the injections. To generate the injection needles, borosilicate capillaries (GC100TF-10, Harvard Instruments) were pulled using Narishige needle puller PN-3 (Narishige Scientific Instrument lab, Japan). Needles were broken against the glass slide and fluid was expelled using an air syringe. Embryos were punctured with a needle containing 30mM CK-666 in DMSO through the lateral epidermis such that the drug could be released roughly in the centre of the yolk cell. DMSO alone was injected into control embryos.

Acknowledgements

We thank Tinri Aegerter and Darren Gilmour for critical reading of the manuscript. This work was supported by a SystemsX.ch grant to DB and CA as part of the MorphogenetiX project and by the Bundesministerium für Bildung und Forschung 031A494 to RSS.

References

- Aristotelous AC, Crawford JM, Edwards GS, Kiehart DP & Venakides S (2018) Mathematical models of dorsal closure. *Prog. Biophys. Mol. Biol.* Available at: <http://linkinghub.elsevier.com/retrieve/pii/S007961071830021X>
- Atzeni F, Lanfranconi F & Aegerter CM (2019) Disentangling geometrical, viscoelastic and hyperelastic effects in force-displacement relationships of folded biological tissues. *Eur. Phys. J. E* **42**: 47 Available at: <https://doi.org/10.1140/epje/i2019-11807-x>
- Azevedo D, Antunes M, Prag S, Ma X, Hacker U, Brodland GW, Hutson MS, Solon J & Jacinto A (2011) DRhoGEF2 Regulates Cellular Tension and Cell Pulsations in the Amnioserosa during Drosophila Dorsal Closure. *PLoS One* **6**: e23964 Available at: <http://dx.plos.org/10.1371/journal.pone.0023964>
- Bambardekar K, Clément R, Blanc O, Chardès C & Lenne P-F (2015) Direct laser manipulation reveals the mechanics of cell contacts in vivo. *Proc. Natl. Acad. Sci.* **112**: 1416–1421 Available at: <http://www.pnas.org/content/112/5/1416%5Cnhttp://www.ncbi.nlm.nih.gov/pubmed/25605934%5Cnhttp://www.pnas.org/content/112/5/1416.full> [Accessed January 21, 2015]
- Bement WM, Leda M, Moe AM, Kita AM, Larson ME, Golding AE, Pfeuti C, Su KC, Miller AL, Goryachev AB & Von Dassow G (2015) Activator-inhibitor coupling between Rho signalling and actin assembly makes the cell cortex an excitable medium. *Nat. Cell Biol.* **17**: 1471–1483
- Blanchard GB, Murugesu S, Adams RJ, Martinez-Arias a. & Gorfinkiel N (2010) Cytoskeletal dynamics and supracellular organisation of cell shape fluctuations during dorsal closure. *Development* **137**: 2743–2752 Available at: <http://dev.biologists.org/cgi/doi/10.1242/dev.045872>
- Brinkmann F, Mercker M, Richter T & Marciniak-Czochra A (2018) Post-Turing tissue pattern formation: Advent of mechanochemistry. *PLoS Comput. Biol.* **14**: 1–21
- Brodland GW & Clausi DA (1995) Cytoskeletal mechanics of neurulation: insights obtained from computer simulations. *Biochem. Cell Biol.* **73**: 545–553 Available at: <http://www.scopus.com/inward/record.url?eid=2-s2.0-0029331863&partnerID=40&md5=b19b93a4ba6d31b75e515fb1b1997d8e>
- Castelli-Gair J, Greig S, Micklem G, Akam M (1994) Dissecting the temporal requirements for homeotic gene function, *Development* 120:1983-1995

- Caussinus E, Kanca O & Affolter M (2012) Fluorescent fusion protein knockout mediated by anti-GFP nanobody. *Nat. Struct. Mol. Biol.* **19**: 117–122 Available at: <http://dx.doi.org/10.1038/nsmb.2180>
- David DJ V, Wang Q, Feng JJ & Harris TJC (2013) Bazooka inhibits aPKC to limit antagonism of actomyosin networks during amnioserosa apical constriction. *Development* **140**: 4719–4729 Available at: <http://www.ncbi.nlm.nih.gov/pubmed/24173807>
- Davidson LA, Koehl MAR, Keller R & Oster GF (1995) How do sea urchins invaginate? Using biomechanics to distinguish between mechanisms of primary invagination. *Development* **121**: 2005–2018 Available at: <http://dev.biologists.org/content/121/7/2005>
- Dobrovinski K, Swan M, Polyakov O & Wieschaus EF (2017) Measurement of cortical elasticity in *Drosophila melanogaster* embryos using ferrofluids. **114**:
- Étienne J, Fouchard J, Mitrossilis D, Bui N, Durand-Smet P & Asnacios A (2015) Cells as liquid motors: mechanosensitivity emerges from collective dynamics of actomyosin cortex. *Proc. Natl. Acad. Sci. U. S. A.* **112**: 2740–5 Available at: <http://www.pnas.org.sire.ub.edu/content/112/9/2740>
- Fernández BG, Arias AM & Jacinto A (2007) Dpp signalling orchestrates dorsal closure by regulating cell shape changes both in the amnioserosa and in the epidermis. *Mech. Dev.* **124**: 884–897
- Fischer SC, Blanchard GB, Duque J, Adams RJ, Arias AM, Guest SD & Gorfinkiel N (2014) Contractile and Mechanical Properties of Epithelia with Perturbed Actomyosin Dynamics. *PLoS One* **9**: e95695 Available at: <http://www.pubmedcentral.nih.gov/articlerender.fcgi?artid=3997421&tool=pmcentrez&rendertype=abstract> [Accessed November 10, 2014]
- Franke JD, Montague RA & Kiehart DP (2005) Nonmuscle myosin II generates forces that transmit tension and drive contraction in multiple tissues during dorsal closure. *Curr. Biol.* **15**: 2208–2221
- Garcia Fernandez B, Martinez-Arias A & Jacinto A (2007) Dpp signalling orchestrates dorsal closure by regulating cell shape changes both in the amnioserosa and in the epidermis. **124**: 884–897
- Gierer A & Meinhardt H (1972) A Theory of Biological Pattern Formation. *Kybernetik* **12**: 30–39
- Harden N, Ricos M, Yee K, Sanny J, Langmann C, Yu H, Chia W & Lim L (2002) Drac1 and Crumbs participate in amnioserosa morphogenesis during dorsal closure in *Drosophila*. *J. Cell Sci.* **115**: 2119 LP-2129 Available at: <http://jcs.biologists.org/content/115/10/2119.abstract>

Hetrick B, Han MS, Helgeson LA & Nolen BJ (2013) Small molecules CK-666 and CK-869 inhibit actin-related protein 2/3 complex by blocking an activating conformational change. *Chem. Biol.* **20**: 701–712 Available at: <https://www.ncbi.nlm.nih.gov/pubmed/23623350>

Holmes WR, Carlsson AE & Edelstein-Keshet L (2012) Regimes of wave type patterning driven by refractory actin feedback: transition from static polarization to dynamic wave behaviour. *Phys. Biol.* **9**: 046005 Available at: <http://stacks.iop.org/1478-3975/9/i=4/a=046005?key=crossref.5b2accd1d45d09ccbe7a3b47a0abae68>

Hunter GL, Crawford JM, Genkins JZ & Kiehart DP (2014) Ion channels contribute to the regulation of cell sheet forces during Drosophila dorsal closure. *Development* **141**: 325–334 Available at: <http://dev.biologists.org/cgi/doi/10.1242/dev.097097>

Jankovics F & Brunner D (2006) Transiently Reorganized Microtubules Are Essential for Zippering during Dorsal Closure in Drosophila melanogaster. *Dev. Cell* **11**: 375–385 Available at: <http://linkinghub.elsevier.com/retrieve/pii/S1534580706003157>

Jayasinghe AK, Crews SM, Mashburn DN & Hutson MS (2013) Apical oscillations in amnioserosa cells: basolateral coupling and mechanical autonomy. *Biophys. J.* **105**: 255–65 Available at: <http://www.pubmedcentral.nih.gov/articlerender.fcgi?artid=3699749&tool=pmcentrez&rendertype=abstract> [Accessed September 1, 2014]

Kiehart DP, Crawford JM, Aristotelous A, Venakides S & Edwards GS (2017) Cell Sheet Morphogenesis: Dorsal Closure in Drosophila melanogaster as a Model System. *Annu. Rev. Cell Dev. Biol. Annu. Rev. Cell Dev. Biol* **33**: 169–202 Available at: <https://doi.org/10.1146/annurev-cellbio-111315-125357202.%0Awww.annualreviews.org>

Kiehart DP, Galbraith CG, Edwards K a., Rickoll WL & Montague R a. (2000) Multiple forces contribute to cell sheet morphogenesis for dorsal closure in Drosophila. *J. Cell Biol.* **149**: 471–490 Available at: <http://www.jcb.org/lookup/doi/10.1083/jcb.149.2.471>

Lada K, Gorfinkiel N & Martinez Arias A (2012) Interactions between the amnioserosa and the epidermis revealed by the function of the u-shaped gene. *Biol. Open* **1**: 353–361 Available at: <http://www.pubmedcentral.nih.gov/articlerender.fcgi?artid=3509461&tool=pmcentrez&rendertype=abstract>

Lu Y & Settleman J (1999) The Drosophila Pkn protein kinase is a Rho/Rac effector target required for dorsal closure during embryogenesis. *Genes Dev.* **13**: 1168–1180 Available at: <https://www.ncbi.nlm.nih.gov/pubmed/10323867>

Machado PF, Duque J, Étienne J, Martinez-Arias A, Blanchard GB & Gorfinkiel N (2015) Emergent material properties of developing epithelial tissues. *BMC Biol.* **13**: 98 Available at: <http://www.biomedcentral.com/1741-7007/13/98>

Martin AC & Goldstein B (2014) Apical constriction: themes and variations on a cellular mechanism driving morphogenesis. *Development* **141**: 1987–1998 Available at: <http://dev.biologists.org/cgi/doi/10.1242/dev.102228>

Mogilner A & Edelstein-Keshet L (2002) Regulation of actin dynamics in rapidly moving cells: A quantitative analysis. *Biophys. J.* **83**: 1237–1258 Available at: [http://dx.doi.org/10.1016/S0006-3495\(02\)73897-6](http://dx.doi.org/10.1016/S0006-3495(02)73897-6)

Munjal A, Philippe J-M, Munro E & Lecuit T (2015) A self-organized biomechanical network drives shape changes during tissue morphogenesis. *Nature* Available at: <http://www.nature.com/doi/10.1038/nature14603>

Murray JD ed. (2004) *Mathematical Biology* New York, NY: Springer New York Available at: <http://link.springer.com/10.1007/b98868>

Ninov N, Menezes-Cabral S, Prat-Rojo C, Manjón C, Weiss A, Pyrowolakakis G, Affolter M & Martín-Blanco E (2010) Dpp Signaling Directs Cell Motility and Invasiveness during Epithelial Morphogenesis. *Curr. Biol.* **20**: 513–520 Available at: <https://linkinghub.elsevier.com/retrieve/pii/S0960982210002149>

Padash Barmchi M, Rogers S & Häcker U (2005) DRhoGEF2 regulates actin organization and contractility in the *Drosophila* blastoderm embryo. *J. Cell Biol.* **168**: 575–585 Available at: <https://www.ncbi.nlm.nih.gov/pubmed/15699213>

Pasakarnis L, Frei E, Caussinus E, Affolter M & Brunner D (2016) Amnioserosa cell constriction but not epidermal actin cable tension autonomously drives dorsal closure. *Nat. Cell Biol.* **18**: 1161–1172 Available at: <http://www.nature.com/doi/10.1038/ncb3420>

Rauzi M, Lenne PF & Lecuit T (2010) Planar polarized actomyosin contractile flows control epithelial junction remodelling. *Nature* **468**: 1110–1115 Available at: <http://dx.doi.org/10.1038/nature09566>

Razzell W, Wood W & Martin P (2014) Recapitulation of morphogenetic cell shape changes enables wound re-epithelialisation. : 1814–1820

Riesgo-Escovar JR & Hafen E (1997) *Drosophila* jun kinase regulates expression of decapentaplegic via the ets-domain protein Aop and the ap-1 transcription factor Djun during dorsal closure. *Genes Dev.* **11**: 1717–1727

Robin FB, Michaux JB, McFadden WM & Munro EM (2016) Excitable RhoA dynamics drive pulsed contractions in the early *C. elegans* embryo. *bioRxiv*

Rotty JD, Wu C & Bear JE (2012) New insights into the regulation and cellular functions of the ARP2/3 complex. *Nat. Rev. Mol. Cell Biol.* **14**: 7

Saias L, Swoger J, D'Angelo A, Hayes P, Colombelli J, Sharpe J, Salbreux G & Solon J (2015) Decrease in Cell Volume Generates Contractile Forces Driving Dorsal Closure. *Dev. Cell* **d**: 1–11 Available at: <http://linkinghub.elsevier.com/retrieve/pii/S1534580715002129>

Segal D, Zaritsky A, Schejter ED & Shilo BZ (2018) Feedback inhibition of actin on Rho mediates content release from large secretory vesicles. *J. Cell Biol.*: 1–12

Sokolow A, Toyama Y, Kiehart DP & Edwards GS (2012) Cell ingression and apical shape oscillations during dorsal closure in *Drosophila*. *Biophys. J.* **102**: 969–79 Available at: <http://www.pubmedcentral.nih.gov/articlerender.fcgi?artid=3296024&tool=pmcentrez&rendertype=abstract> [Accessed November 4, 2014]

Solon J, Kaya-Copur A, Colombelli J & Brunner D (2009) Pulsed forces timed by a ratchet-like mechanism drive directed tissue movement during dorsal closure. *Cell* **137**: 1331–42 Available at: <http://www.ncbi.nlm.nih.gov/pubmed/19563762> [Accessed July 12, 2014]

Tsuneizumi K, Nakayama T, Kamoshida Y, Kornberg TB, Christian JL & Tabata T (1997) Daughters against dpp modulates dpp organizing activity in *Drosophila* wing development. *Nature* **389**: 627–631 Available at: <https://doi.org/10.1038/39362>

Turing AM (1952) The Chemical Basis of Morphogenesis. *Philos. Trans. R. Soc. Lond. B. Biol. Sci.* **237**: 37–72 Available at: <http://www.jstor.org/stable/92463>

West JJ, Zulueta-Coarasa T, Maier JA, Lee DM, Bruce AEE, Fernandez-Gonzalez R & Harris TJC (2017) An Actomyosin-Arf-GEF Negative Feedback Loop for Tissue Elongation under Stress. *Curr. Biol.* **27**: 2260–2270.e5 Available at: <http://dx.doi.org/10.1016/j.cub.2017.06.038>

Wodarz A, Hinz U, Engelbert M & Knust E (1995) Expression of crumbs confers apical character on plasma membrane domains of ectodermal epithelia of *Drosophila*. *Cell* **82**: 67–76

Zahedi B, Shen W, Xu X, Chen X, Mahey M & Harden N (2008) Leading edge-secreted Dpp cooperates with ACK-dependent signaling from the amnioserosa to regulate myosin levels during dorsal closure. *Dev. Dyn.* **237**: 2936–2946 Available at: <https://doi.org/10.1002/dvdy.21722>

Figure 1: F-actin oscillation are Myosin-independent and Arp2/3 dependent

A) Comparison of F-actin dynamics wild type (upper row) and MyoII activity-depleted amnioserosa cells (lower row). Scale bars: 20 μm . B) Quantification of F-actin dynamics comparing wild type and MyoII activity-depleted amnioserosa cells. C) F-actin oscillations in homozygous mutants of the myosin heavy chain gene *zip1*. Scale bars: 10 μm . D) F-actin oscillations in MyoII activity-depleted amnioserosa cells injected with DMSO only or with the Arp2/3 inhibiting drug CK666 dissolved in DMSO. Scale bars: 10 μm

Figure 2: Modelling Myosin-independent F-actin oscillation with reaction-diffusion equations

A) The mesh generation procedure: AS cells were manually segmented starting from the maximum projection of a SPIM image and a strip of epidermis (ES) was arbitrarily defined around the AS; the mechanical mesh was computed for both AS and ES tissues; the biochemical mesh was computed as a subdivision of the mechanical mesh for AS only. B) Reaction diagram for F-actin dynamics in the model. Pointed arrows indicate positive feedback, constant or linear reaction. Capped arrows indicate negative feedback. C) F-actin conc. at multiple time steps in absence of myosin activity. D) Fraction of cells in each F-actin activity category over time. E) parameter screens statistics, left to right: relative amplitude and period of cells' F-actin oscillation; passive and locally active fraction of cells at equilibrium. Each plot shows average values over all AS cells and time steps, with contour lines calculated with MATLAB's contour function, starting from measures of simulation runs (red circles).

Figure 3: Simulations provide interpretation for WT and perturbed in vivo phenotypes

A) Schematic representation of contractility calculation: first, F-actin conc. is calculated on the biochemical mesh; then, the concentration is extrapolated to the larger mechanical triangles; last, mechanical forces and corresponding deformation are calculated. B) Cell area and F-actin over time for 3 cells at the center of the opening. C) F-actin conc. at multiple time steps with myosin activity. D, E) parameter screens statistics, when varying production rates of ANPa and ANPi (D), and the contractility parameters c_{Max} and c_{Fthr} (E). Statistics plot are, left to right: relative amplitude and period of cell area oscillation; inactive and locally active fraction of cells at equilibrium; fraction of in-phase neighbor oscillations. Each plot shows average values over all AS cells and time steps, with contour lines calculated with MATLAB's contour function, starting from measures of simulation runs (red circles).

Figure 4: ES Tissue relaxation mediating Dpp-independent AS tissue contraction

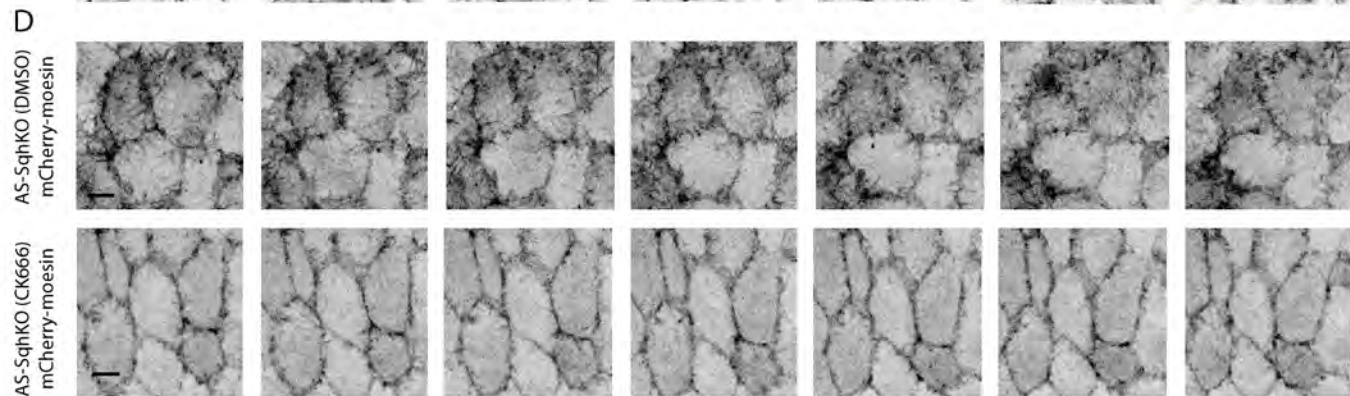
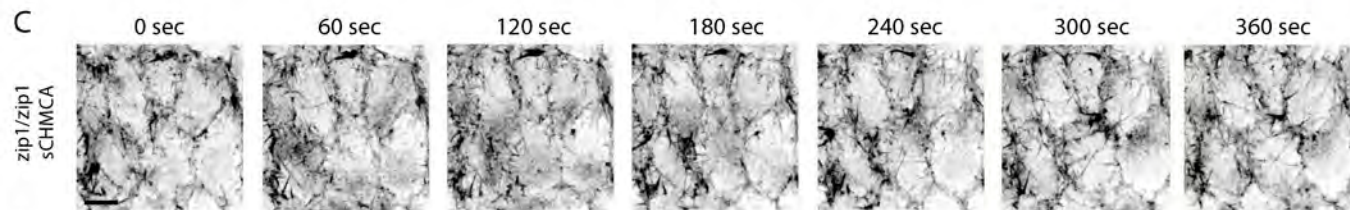
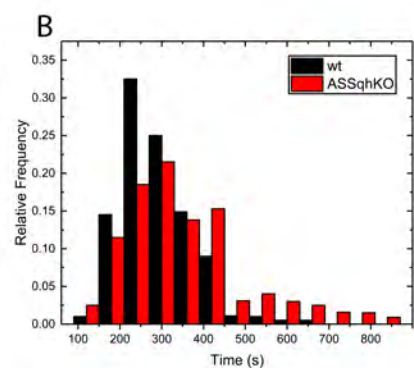
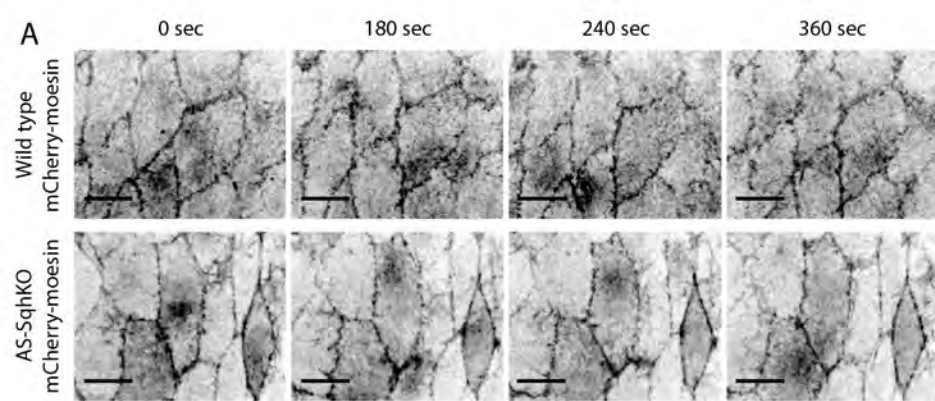
A) Choice of ES regions with isotropic and anisotropic material relaxation. B) AS tissue area dynamics with different relaxation time constants. C) Cell area oscillations (blue) in correlation with F-actin concentration dynamics (red) for 3 randomly chosen cells (solid, dashed and dotted lines). D) Sub-cellular F-actin concentration dynamics at indicated time points in a simulation including Myosin activity and ES material relaxation. E) As tissue-specific interference with Dpp signalling gradient by overexpression of constitutively active Dpp receptor thickveins (tkv^{act} , second column) or the signalling inhibitor Dad (third column) in embryos expressing nuclear GFP under control of the Dpp responsive dad promoter to visualise cellular Dpp signalling activity levels. In all cases closure occurs similar to the wild type (first column).

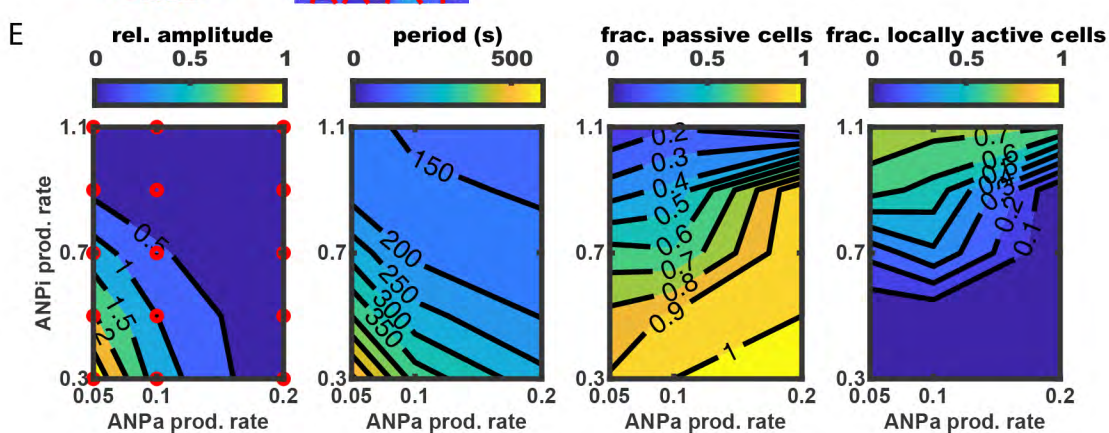
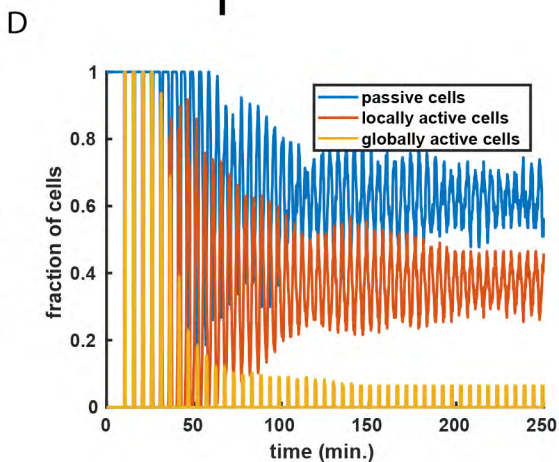
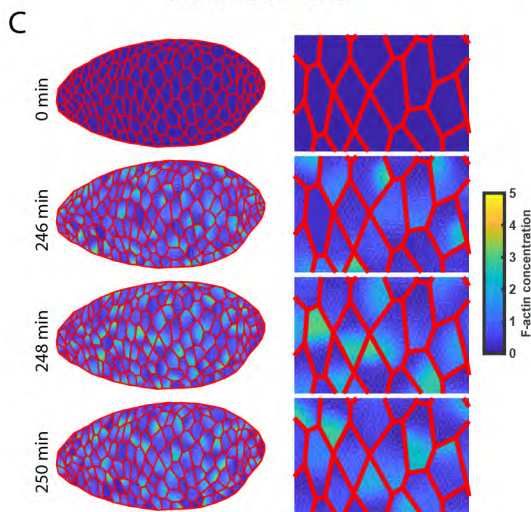
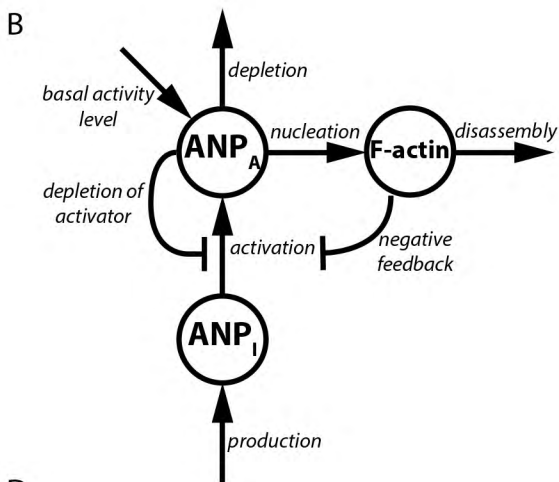
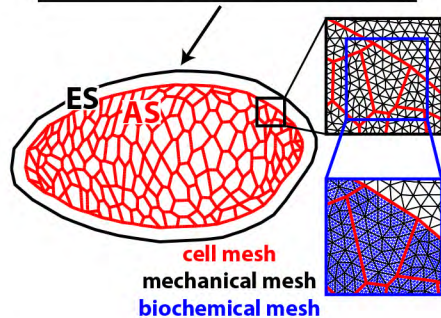
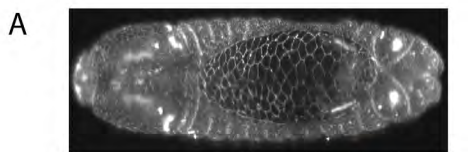
Figure 5: Exploring ES and AS properties reveals emergent cell patterning and tissue shaping

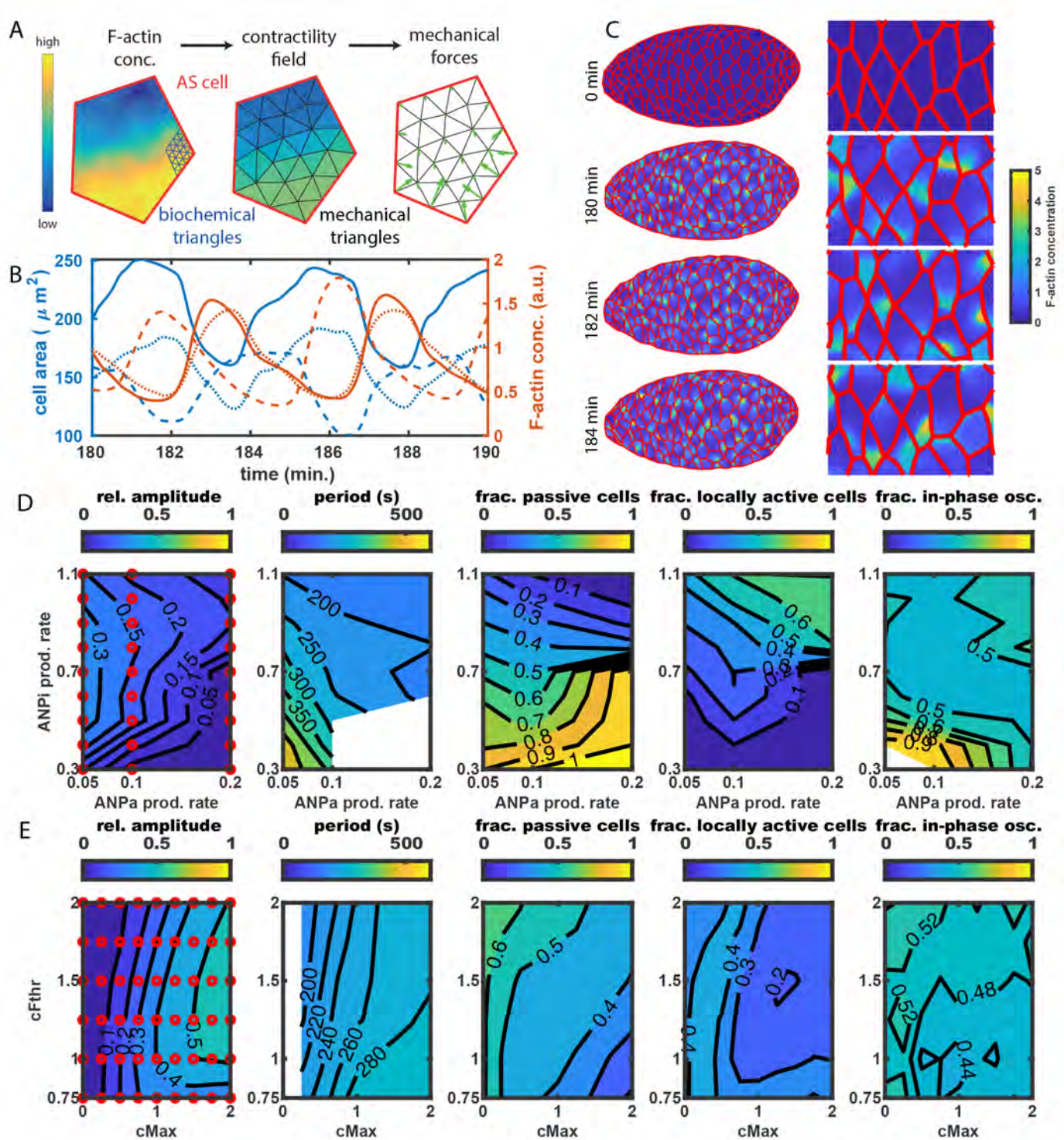
A,B,D) initial AS cells geometry with cells coloured according to their arrest time as parameters are varied: A, varying $cMax$ and $cFthr$; B, varying α and β ; E, varying epidermis width and ES stiffness. Colour scale minimum and maximum are set for each simulation as the earliest and latest arresting cell time of that simulation. Cells in white do not arrest within the simulated time. C,D) Snapshots over time with larger epidermis along the AP (C) and DV (D) axis. E) Snapshots over time with larger epidermis along the DV axis and a computer-generated AS tissue discretisation in which AS cells are all almost equal to each other.

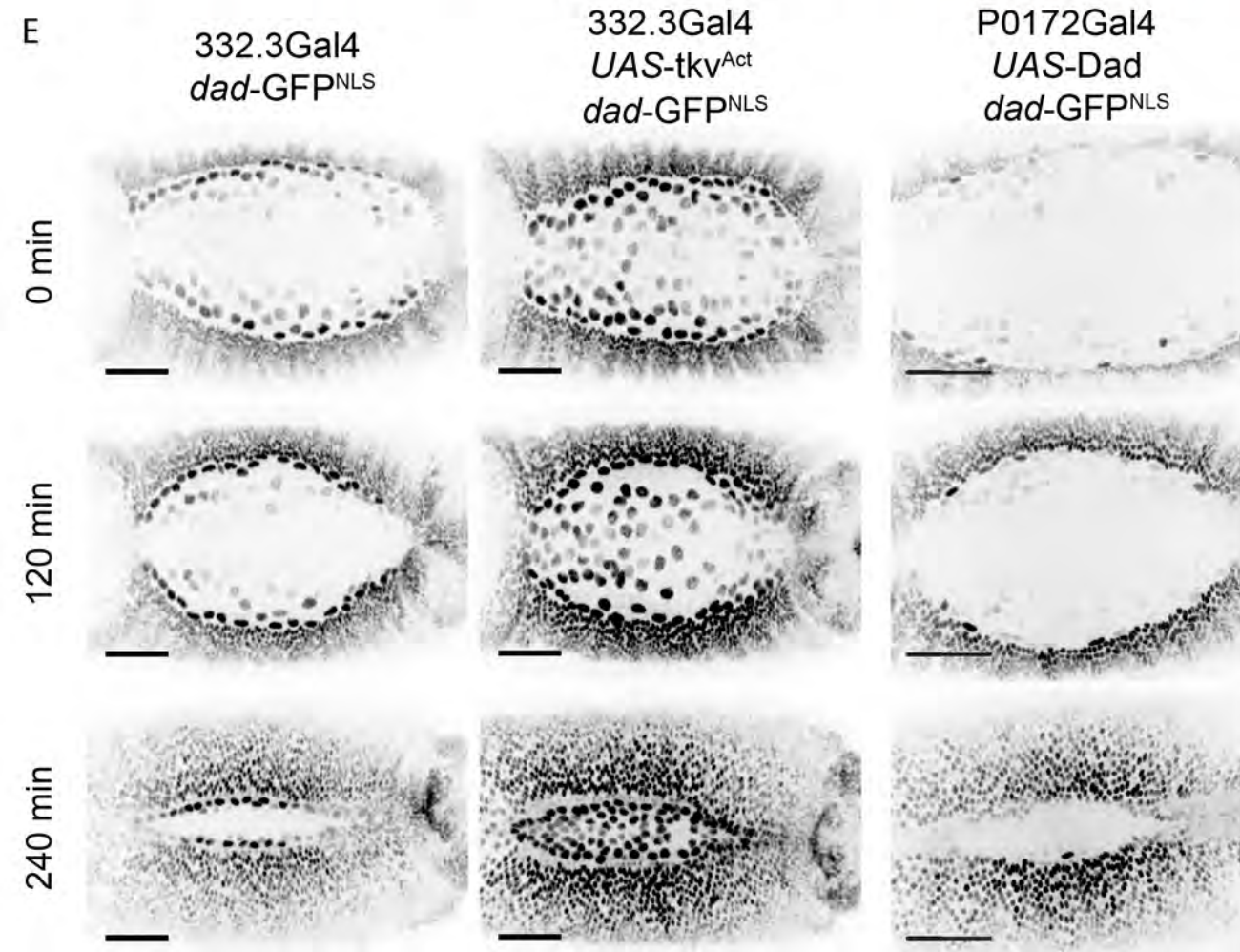
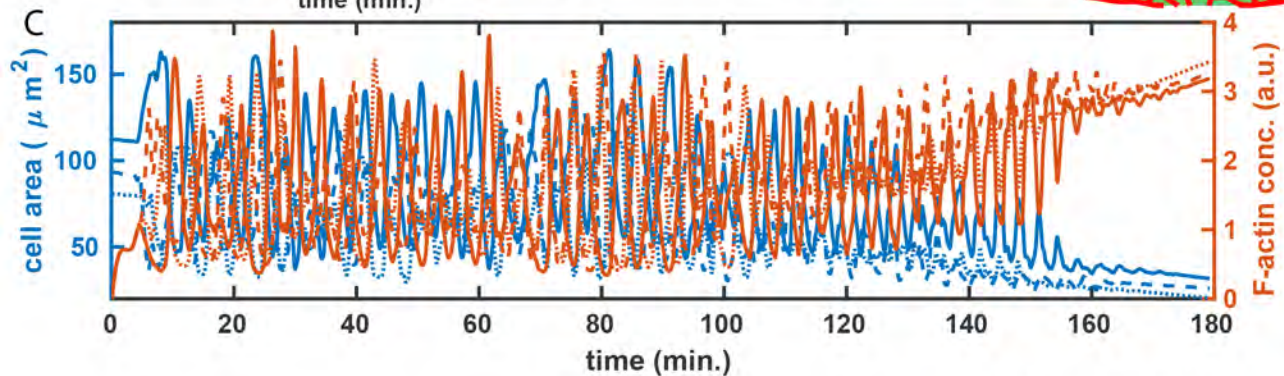
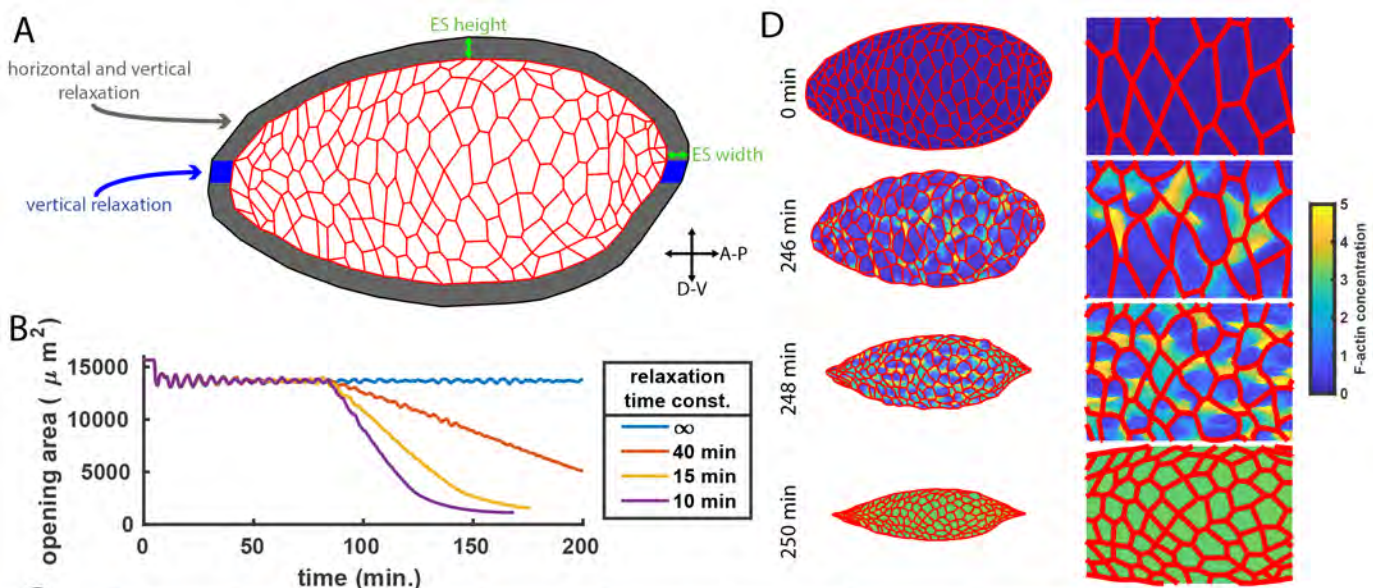
Figure 6: Simulations phenocopy wild type and mutant scenarios

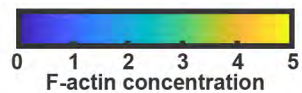
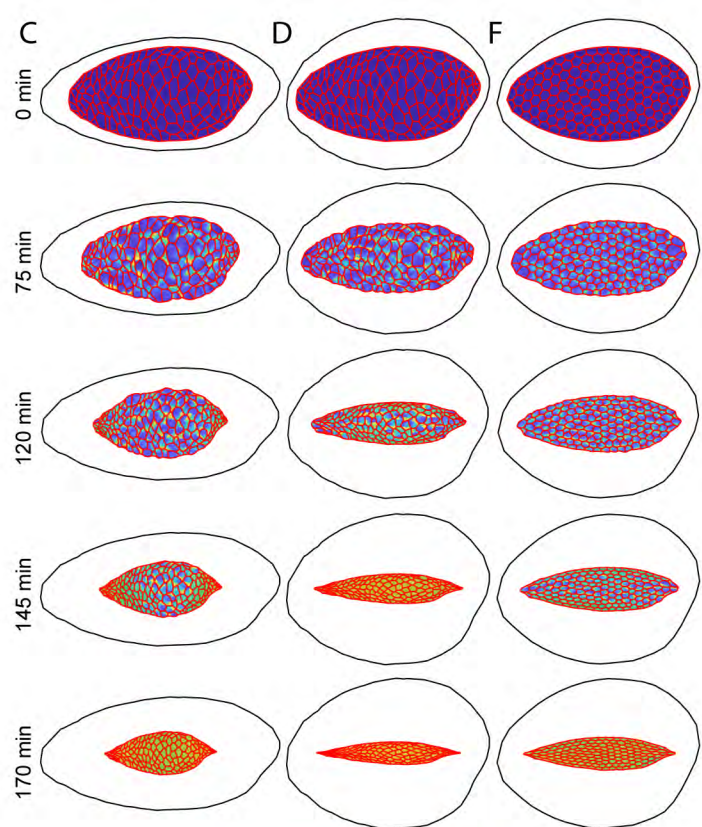
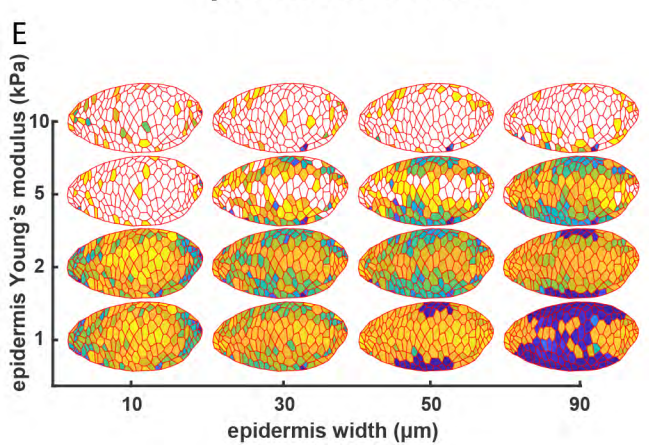
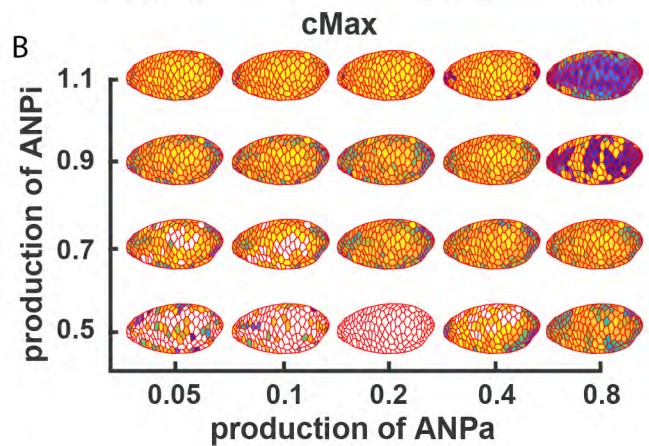
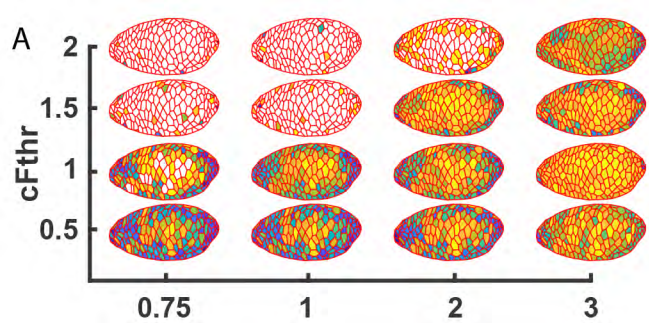
A) initial geometry, cropped region (black square) and colour-scale of all subsequent time snapshots, chosen to show oscillatory dynamics. Simulations correspond to: B) wild type (same parameters as Fig. 2C,D); C) embryos with expression of $ctMLCK$ (same parameters as B, except $cFthr = 1$, $cMax = 2.5$); D) embryos with expression of $MbsN300$ or maternal mutant for $DRhoGEF2$ (same parameters as B, except $cMax = 0.2$); E) embryos with $DRhoGEF2$ over-expression (same parameters as B, except $cMax = 2$).

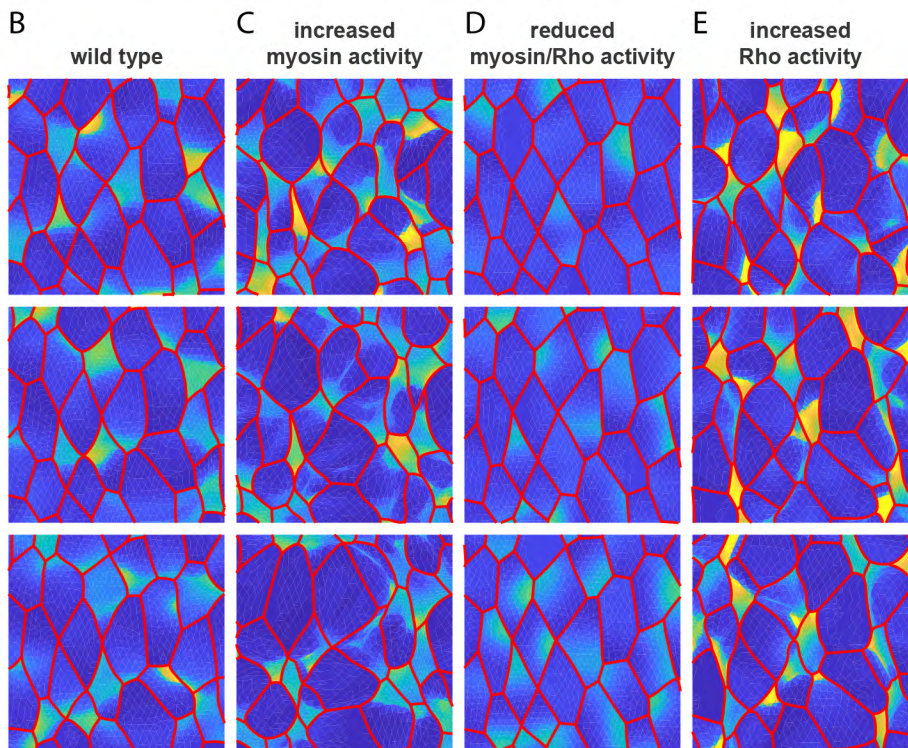
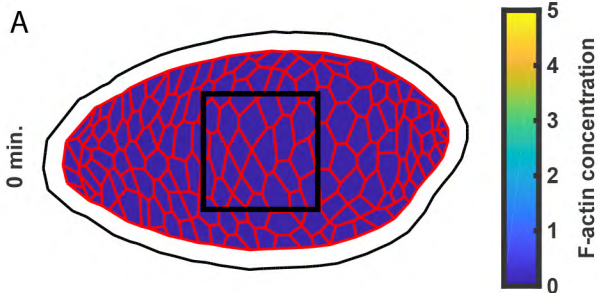












Supplementary Material to "Mechanochemical modelling of dorsal closure reveals emergent cell behaviour and tissue morphogenesis"

Francesco Atzeni, Laurynas Pasakarnis, Dominika Tworus, Gabriella Mosca,
Richard S. Smith, Christof M. Aegerter and Damian Brunner

1 Modelling background

Modelling dorsal closure with reaction-diffusion equations coupled to cell and tissue scale force generation was influenced by a number of other approaches. Here, we discuss the most relevant models of dorsal closure, as well as models of other systems that were fundamental for the development of our approach.

Here we focus on a selection of models, selected for their conceptual or technical influence on our work. The reader interested in a comprehensive review of modelling of dorsal closure is referred to [Aristotelous et al., 2018]. A vertex model with cell-scale force coordination, developed by Solon et al. [Solon et al., 2009] addressed the ratchet-like role of the actin cable during closure. Even though AS cell constriction has now been shown to be the driving force of DC [Pasakarnis et al., 2016], the approach of Solon et al. is interesting because it shows that patterns of neighbouring cell coordination may emerge in simulations even though no chemical coupling between cells is implemented. Notably, Solon et al. relies on tension-driven contractility for oscillations to emerge, hence representing mechanical coupling between cells which goes beyond simple attachment. The vertex model of Solon et al. was extended by Wang et al. [Wang et al., 2012]. In their model, each cell was subdivided in a discrete number of biomechanical units. On each unit, the dynamics of idealised signalling molecules leading to myosin-driven contraction were modelled. Notably, [Wang et al., 2012], as well as the more recent [Dierkes et al., 2014, Lo et al., 2018], albeit to different levels of technical sophistication, show that oscillations emerge through coupling of an idealised signalling network with linear or non-linear elastic behaviour. While such models consider how the dynamics of sub-cellular structures lead to dynamics at the tissue scale, another interesting ap-

proach has been to describe dorsal closure at the scale of the AS and ES tissues [Almeida et al., 2011]. In particular, they consider a continuum material description of AS and ES, implementing tissue-scale forces driving closure, namely epidermal tension, actin cable tension, amnioserosa contraction and zipping and describing each with a single coefficient. Interestingly, fitting those coefficients to the behaviour of wild type embryos and embryos without zipping, they are able to reproduce the different shapes of amnioserosa during closure of those scenarios. A continuum material description was also used by [Hutson et al., 2009], who developed a cell-level finite element model and parametrised simulations to match the material response to laser hole drilling *in vivo*.

Our approach integrates a continuum epidermis description, with a continuous description of individual AS cells. Based on our experimental evidence, the formation of transient F-actin structures does not rely on mechanical coupling. Hence, for each AS cell, we model F-actin dynamics that lead to F-actin oscillations, which are realised through sub-cellular F-actin structures. We also assume that the exact location of F-actin structures in a cell is not controlled by an upstream polarisation event. That is, we model a spontaneous patterning event leading to the formation of F-actin structures and include a mechanism whereby the F-actin structures form and disassemble periodically over time.

We translate the conceptual model of oscillating pattern formation into reaction-diffusion equations. The reaction-diffusion mechanism, as conceived by Alan Turing in 1952 [Turing, 1952], states that two substances with different diffusion rates and subject to noise in their concentration may produce spatially heterogeneous concentration profiles (called patterns) even though they are initially uniformly distributed. While Turing himself suggested that the simulated spontaneous patterns may be related to patterns observed *in vivo*, it was only in the 1970-80s that the reaction-diffusion mechanism started to be seen as a mechanism that biological organisms may actually employ. This is largely due to the work of Alfred Gierer and Hans Meinhardt, who decided to employ computer simulations of pattern formation to understand the patterning events in *Hydra* [Meinhardt, 2006]. Hence, they parametrised reaction-diffusion systems to reproduce specific scenarios and, importantly, defined precise requirements for the reaction part of the equations. They showed that the fast-diffusing component needs to be self-activating, while at the same time an antagonistic reaction needs to be taking place on a longer range [Gierer and Meinhardt, 1972, Meinhardt, 2008]. They proposed two different mechanisms whereby this may be occurring. The most popular of the two is the so-called activator-inhibitor system, which consists in the most intuitive application of short-range activation, long-range inhibition. Alternatively, the antagonistic reaction may occur through substrate depletion, leading to the so-called activator-depleted substrate mechanism

[Gierer and Meinhardt, 1972].

Both mechanisms have been used to model spontaneous pattern formation in a huge variety of biological problems, describing systems ranging from chemical kinetics to population dynamics (reviewed in [Meinhardt, 2008, Volpert and Petrovskii, 2009]). Reaction-diffusion systems have not only been used to model patterning events on static domains, but also on deforming structures. Notably, already in the 1980s time-dependent domain size was included as a parameter in reaction-diffusion systems [Arcuri and Murray, 1986]. Since then many works have considered the effect of growing domains on the emerging stable patterns [Murray, 2002, Murray, 2003]. Generally, domain deformations have been imposed, but recently reaction diffusion equations have also been used to determine the forces that lead to deformation, and have even included mechanical feedback on biochemical dynamics (e.g. [Ruiz-Baier et al., 2014, Ruiz-Baier, 2015, Mercker et al., 2016, Brinkmann et al., 2018]).

Models that include mechanics and biochemical dynamics, which we refer to as mechanochemical, are powerful explorative tools that make quantitative predictions, a desirable feature of any mathematical model [Penders et al., 2008]. On the negative side, mechanochemical models are much more complicated than a model that is only mechanical or only biochemical. Theoretical approaches are generally very limited when it comes to addressing such coupled systems, so that one has to resort to numerical simulations. Such simulations though, need sophisticated numerical algorithms that ensure accurate calculation of the mechanical as well as of the biochemical equation solutions. A powerful, flexible approach to implement mechanochemical models is the finite element method.

The finite element method has a history of application to biology that dates back at least to the 90s (e.g. [Brodland and Clausi, 1994, Davidson et al., 1995]). In recent years, the finite element method has also been used in implementations that include mechanics and force, in modelling of cardiac contractions [Cherubini et al., 2008, Tracqui et al., 2008, Ruiz-Baier, 2015], as well as morphogenesis and growth [Brodland and Veldhuis, 2012, Madzvamuse and Zenas George, 2013, Liu, 2014, Bassel et al., 2014]. To the best of our knowledge, our FEM-based framework is the first to implement continuous biochemical modelling similar to that of [Ruiz-Baier, 2015] in each AS cell, combined with a cell-based continuously elastic tissue description, such as [Hutson et al., 2009, Brodland and Veldhuis, 2012].

2 Development of reaction-diffusion system

In this section we show how we developed our model equations and how parameter values were found.

The original model equations from the classical paper by Gierer and Meinhardt [Gierer and Meinhardt, 1972] read

$$\begin{aligned}\frac{dI}{dt} &= \gamma (\beta - IA^2), \\ \frac{dA}{dt} &= \gamma (\alpha - A + IA^2),\end{aligned}\tag{1}$$

or, with the inclusion of saturation,

$$\begin{aligned}\frac{dI}{dt} &= \gamma (\beta - \Phi(A, I)), \\ \frac{dA}{dt} &= \gamma (\alpha - A + \Phi(A, I)), \\ \Phi(A, I) &= IA^2 \left(\frac{1}{1 + (\frac{A}{A_t})^2} \right).\end{aligned}\tag{2}$$

In the original model A and I represent an activator species and a depleted substrate. That is, the substrate, produced at a constant rate, is activated, or, used up in the activation, with a threshold for the activator of A_t . The active component A is also produced at a ground rate, though much lower than that of I , and degrades linearly.

Even in the absence of a spatial component, the system can be interpreted as describing the dynamics of protein activation. Let's consider the example of an epithelial cell, with its apical and basolateral domains, and model the protein dynamics on the apical domain. Then, the ground production rates shall be interpreted as the combination of actual protein synthesis (in the apical domain or elsewhere) and transport to the apical domain. Protein activation naturally refers to the activation of the inactive protein on the apical domain.

Not only we are interested in the activation dynamics of ANPs (actin nucleation proteins) taking the role of A , but also in their regulation of filamentous actin structures. In particular, we assume that G-actin is abundant in the proximity of the cells apical domain, and that the modelled ANPs represent the dynamics of the various proteins involved in actin filament nucleation and polymerisation. So, we assume that F-actin concentration, F , increases in presence of activated ANPs and then degrades. Further, we assume that ANP activation slows down once F-actin concentration is above a certain threshold, leading to

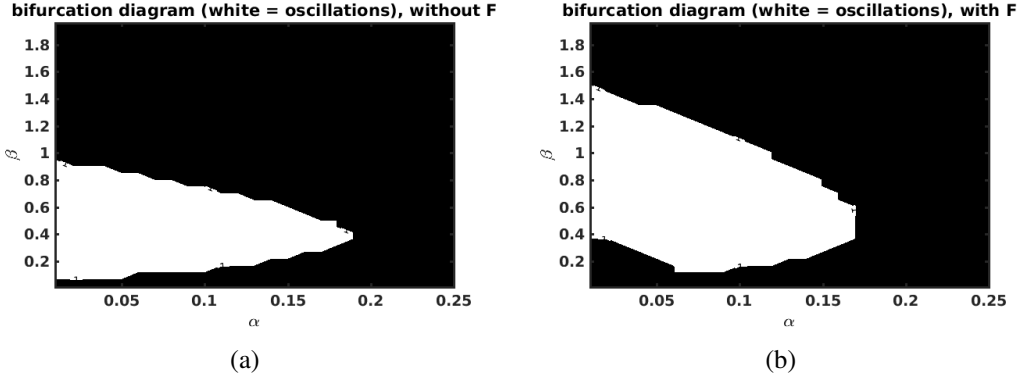


Figure 1: Qualitative behaviour of diffusion-free system: oscillations (white region) and convergence to steady state (black), for Equation 2 (1a) and Equation 3 (1b)

$$\begin{aligned}
 \frac{\partial I}{\partial t} &= \gamma (\beta - \Phi(A, I, F)), \\
 \frac{\partial A}{\partial t} &= \gamma (\alpha - A + \Phi(A, I, F)), \\
 \frac{\partial F}{\partial t} &= \gamma r_1 (A - F),
 \end{aligned} \tag{3}$$

$$\Phi(A, I, F) = IA^2 \left(\frac{1}{1 + (\frac{A}{A_t})^2} - \frac{1}{1 + (\frac{F_t}{F})^2} \right),$$

where F_t is a threshold concentration for F-actin. Including F , enlarges the region of $\alpha - \beta$ parameter space where the systems exhibits oscillations (Figure 1). Before moving to considerations that involve the concentration dynamics in space, we fix the parameter values for this system. In particular, we choose r_1 , F_t and γ so that the period of oscillations is around the experimentally measured value of ≈ 4 minutes.

Then, we include a spatial dependence to the problem by adding diffusion to our equations, which leads to

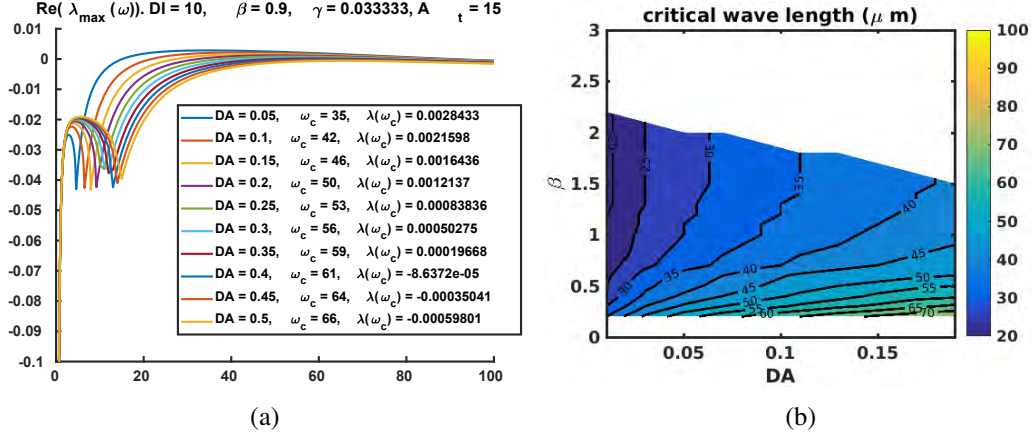


Figure 2: 2a) Plot of the largest eigenvalue as a function of wave-length, as D_A is varied. The critical wave-length is the wave-length at which the largest eigenvalue is maximal. 2a) critical wave length as D_A and β are varied. Parameter regions in which the largest eigenvalue is always negative, corresponding to no spontaneous pattern emergence are white.

$$\begin{aligned}
 \frac{\partial I}{\partial t} &= \gamma(\beta - \Phi(A, I, F)) + D_I \Delta I, \\
 \frac{\partial A}{\partial t} &= \gamma(\alpha - A + \Phi(A, I, F)) + D_A \Delta A, \\
 \frac{\partial F}{\partial t} &= \gamma r_1(A - F) + D_F \Delta F,
 \end{aligned} \tag{4}$$

$$\Phi(A, I, F) = IA^2 \left(\frac{1}{1 + (\frac{A}{A_t})^2} - \frac{1}{1 + (\frac{F}{F_t})^2} \right).$$

In the absence of mechanical coupling, AS cells show localised F-actin that covers only part of their apical surface (Figure 1, main text). To choose the actual diffusion coefficients, a literature search showed that a reasonable value for the diffusion coefficient of ANPi is $10\mu\text{m}^2/\text{s}$. Then, we set the diffusion coefficient of ANPa through linear stability analysis (Figure 2), aiming to reproduce the F-actin pattern features of the myosin (MyoII) mutant. We choose $D_A = 0.1\mu\text{m}^2/\text{s}$, so that the preferred wave length is approximately $40\mu\text{m}$ (and $\beta = 0.7$ or 0.9 , Figure 2b), corresponding to most cells exhibiting one region with high F-actin (see Figure 1, main text). We also use $D_F = 0.001\mu\text{m}^2/\text{s}$, as in numerical simulations the smoother F-actin fronts compared to $D_F = 0\mu\text{m}^2/\text{s}$ lead to smoother contractile fields across mechanical finite elements, which in turn facilitate mechanical convergence.

In wild type, myosin would bind to F-actin structure generating contractile forces. We postpone

the considerations on contractile force generation to later stages, and here only consider the effect of geometrical changes on actin dynamics. We assume that ANPi is produced at a constant amount as the cell area varies, or, equivalently, that the linear concentration increase of ANPi is inversely proportional to cell area. Hence, the final system of reaction-diffusion equations reads

$$\begin{aligned}
\frac{\partial I}{\partial t} &= \gamma \left(\beta \frac{S_0}{S_t} - \Phi(A, I, F) \right) + D_I \Delta I, \\
\frac{\partial A}{\partial t} &= \gamma (\alpha - A + \Phi(A, I, F)) + D_A \Delta A, \\
\frac{\partial F}{\partial t} &= \gamma r_1 (A - F) + D_F \Delta F, \\
\Phi(A, I, F) &= IA^2 \left(\frac{1}{1 + (\frac{A}{A_t})^2} - \frac{1}{1 + (\frac{F}{F_t})^2} \right).
\end{aligned} \tag{5}$$

With the inclusion of the ratio of initial cell area to current area $\frac{S_0}{S_t}$, the system of reaction-diffusion equations becomes effectively coupled to the mechanical simulation. At this point, analytical methods can not be used to exactly determine the behaviour of the system. Under simplifying assumptions, though, it is still possible to roughly predict its qualitative behaviour. In particular, assuming that the concentration across a cell surface is uniform, the stability of the steady state can be calculated with similar methods as in subsection 4.1 above. Doing so, we find that the steady state is oscillatory above a certain value of cF_{thr} , for any given value of $cMax$ (Figure 3a). Albeit the uniform-concentration assumption impedes quantitative interpretation of the diagram, it still predicts that oscillating F-actin oscillations leading to cell area oscillations are to be expected.

When cells exhibit F-actin and cell area oscillations, they are able to produce transient contractile forces. Indeed, if cells can shrink more and more over contractile cycles, they would on average reduce their surface area S_t over time. Since ANPi-production amount was assumed to be independent of cell area, as S_t decreases, the ANPi production rate $\beta \frac{S_0}{S_t}$ increases, which corresponds to an increase in β if the area dependence is omitted (Figure 3b). Since the value of F at steady state increases as β increases and since contraction starts above a threshold value of F , cells will eventually be able to shrink even when the system is at steady state and does not exhibit an inhomogeneous spatial pattern (increasing β leads to absence of spatial pattern, see Figure 2b). This means that as closure proceeds, cell area oscillations driven by F-actin patterning are expected to arrest (Figure 3b) in favour of high, homogeneous F-actin concentration corresponding to cell-wide contractions.

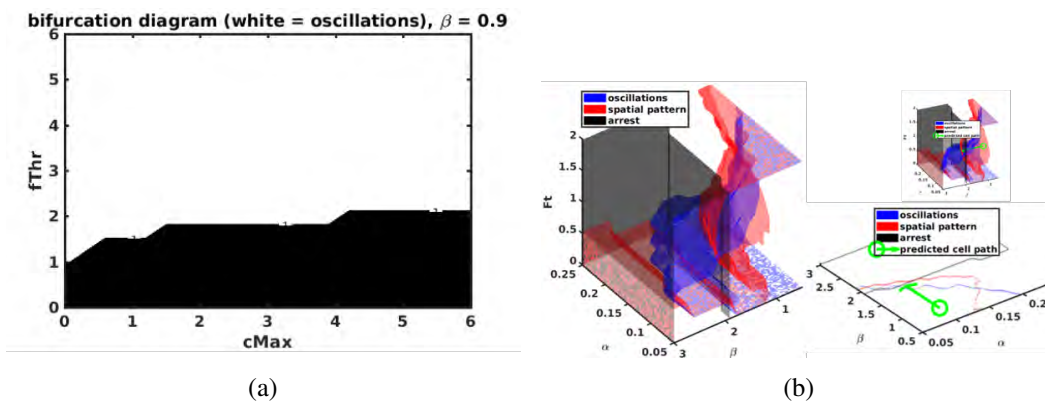


Figure 3: 3a) qualitative behaviour of steady state of Equation 5, under some limiting assumptions discussed in the text. The state is oscillatory in the white region and stable in the black one. 3b) Different representations of oscillatory, spontaneous patterning and oscillation arrest region, as parameters are varied. The boundary of the oscillations region is from Figure 1b, that of the spontaneous patterning region is from Figure 2b and the arrest region is such that the value of F-actin at steady state is above the contraction threshold ($F^* = \alpha + \beta > cFthr = 2$).

3 The mechanochemical simulation

3.1 Implementation of reaction-diffusion system

To solve the reaction-diffusion method on the deforming mesh, we chose a numerical scheme that can handle deforming meshes, while still being reasonably computationally efficient. Our approach is based on a surface finite-element method first developed to solve partial differential equations on surfaces whose evolution is imposed over time [Dziuk and Elliott, 2007]. The original implementation integrates both the reaction and the diffusion parts implicitly, while in subsequent adjustments, reactions have also partially or completely been explicitly integrated [Barreira et al., 2011, Elliott et al., 2012, Murphy et al., 2016].

We implement an implicit-explicit time-stepping scheme for the temporal approximation, in which diffusion is implicitly integrated, and reaction is explicitly integrated (as in [Murphy et al., 2016]). We choose to integrate the reaction component forward in time for two reasons. First, it allows implementing new reaction functions without adjusting the discretisation of the system. Second, it allows solving separately for each species of the system. Explicit integration of the reactions, though, requires a smaller time step compared to implicit integration. We validated our approach for one of the reaction-diffusion mechanisms by varying the time step (subsection 3.5).

Adapting the derivation in [Barreira et al., 2011] to explicit time stepping, the approximation reads

$$(\mathcal{M}(t^{m+1}) + \tau D_i \mathcal{K}(t^{m+1})) u_i^{m+1} = \mathcal{M}(t^m)(u_i^m + \tau \mathbf{F}_i(\mathbf{u}^m)), \quad (6)$$

where τ is the time step, $\mathcal{M}(t)$ and $\mathcal{K}(t)$ are the time-dependent surface mass and stiffness matrices, D_i is the diffusion coefficient of species i , \mathbf{u}^m is the vector of nodal values at time t^m and u_i^m its i^{th} entry, F are the reaction kinetics. In order to facilitate spontaneous pattern emergence across parameter choices, we added Gaussian noise with mean 0 and standard deviation 0.05 to the concentration of I at each time step. The equilibrium distributions do not depend on the noise amplitude.

3.2 The mechanical implementation

The calculation of mechanical equilibrium is the same as in the original implementation by Richard Smith's group [Bassel et al., 2014, Mosca, 2016], the only difference being the convergence criterion. In this work, we used a threshold for maximal displacement ratio, whereby the mechanical iteration has converged when the relative increase in the vertex displacement norm is below a threshold. The original FEM program was developed to simulate growth of 3D plant cells.

Growth was implemented as a change in the reference configuration of the triangular elements. We follow the same approach to implement contractility, which we will discuss in the next section. We also use the reference configuration to implement material relaxation, which we discuss here.

In essence, visco-elastic behaviour is implemented assuming a time dependence of the reference configuration. A model of stress relaxation describes the evolution of rest lengths (l_0) as a function of current lengths (l) as $dl_0/dt = k(l - l_0)$, where k is the relaxation rate [Noll et al., 2017].

To extend the model to 2D, consider the deformation gradient \mathbf{F} between reference and current configuration. Using polar decomposition, \mathbf{F} can be written as $\mathbf{F} = \mathbf{V}\mathbf{R} = \mathbf{R}\mathbf{U}$, where \mathbf{R} is a rotation matrix, and \mathbf{U}, \mathbf{V} are scale tensors. Isotropic adaptation can then be achieved by damping the scale tensor \mathbf{U} as

$$\mathbf{U}_{damp} = I + k(\mathbf{U} - I),$$

where k sets the timescale of stress adaptation. The map $\mathbf{F}_{damp} = \mathbf{R}\mathbf{U}_{damp}$ applied to the reference configuration gives the new reference configuration (Figure 4a). Furthermore, the model can be generalised to anisotropic adaptation. Suppose the material adaptation rates along perpendicular unit vectors ξ and ξ_{\perp} are k_1 and k_2 , respectively. Let \mathbf{Q} be a rotation matrix s.t. $\mathbf{Q}\xi = (1, 0)$ and $\mathbf{K} = \begin{pmatrix} k_1 & 0 \\ 0 & k_2 \end{pmatrix}$. Then,

$$\mathbf{F}_{damp} = (I + (\mathbf{V} - I)\mathbf{Q}^T\mathbf{K}\mathbf{Q})\mathbf{R}.$$

To calculate the actual timescale, we can analytically solve

$$dl_0/dt = k(l - l_0)$$

for fixed l - a scenario often referred to as a relaxation experiment. The time solution is given by

$$l_0(t) = c_1 + c_2e^{-kt}.$$

Setting $l_0(0) = r_0$ and $l_0(t) \rightarrow l$ as $t \rightarrow \infty$ yields,

$$l_0(t) = l - r_0\epsilon_0e^{-kt}.$$

Hence, the fraction of reversible deformation can be expressed as $\epsilon_{\text{BACK}} = \epsilon_0e^{-kt}$. Recall that for a Maxwell material $\epsilon_{\text{BACK}} = \epsilon_0e^{-\frac{E}{\eta}t}$. Further, the relaxation time constant is defined as $\tau \equiv \frac{\eta}{E}$, so $\tau = 1/k$. Relaxation is implemented on discrete time units, hence $\tau = \frac{\text{timestep}}{\text{adaptationRate}}$, and $k = \frac{\text{adaptationRate}}{\text{timestep}}$.

We tested our implementation against the analytical solution of Maxwell-like relaxation and found very good agreement.

3.3 Implementing active material behaviour

Material contractility is locally determined by the concentrations of one of the reaction-diffusion equations species. We used two different reaction-diffusion equation models that are presented in the following sections, together with their results when coupled to force generation. In both scenarios, contractility is determined by F-actin, which we simply refer to as F .

Two approaches for integrating active material behavior are commonly employed: active stress and active strain. Active stress consists of an additive decomposition of the stress, or directly of the local forces. Differently, the active strain framework postulates the existence of an additional configuration, often called active configuration, which leads to a multiplicative decomposition of the deformation tensor or of the strain. The latter approach has initially been employed for growth [Rodriguez et al., 1994], and more recently also for contractility [Ruiz-Baier et al., 2014].

Active material contraction is implemented following the active strain approach [Ambrosi and Pezzuto, 2012]. That is, the deformation gradient is multiplicatively decomposed as $\mathbf{F} = \mathbf{F}_e \mathbf{F}_a$ (Figure 4b). The active part defines a stress free configuration that is used to calculate the elastic stresses. In turn, \mathbf{F}_a is driven by the contractility field c , which we calculate as a function of F as

$$c(F(\mathbf{x})) = 1 + c\text{Max} \cdot \frac{F(\mathbf{x})^n}{cF\text{thr}^n + F(\mathbf{x})^n}, \quad (7)$$

with a maximum contractility $c\text{Max}$ and an F-actin threshold concentration for contractility given by $cF\text{thr}$. In the interest of simplicity, we assume that c scales the finite element rest configuration isotropically. Since F is calculated on the finer RDE mesh, its value on each mechanical triangle is averaged. Then, the active configuration is obtained by dividing each rest length by the value of c on that element.

3.4 Simulation structure

The model is implemented in our in-house finite element program. We started developing our coupled approach from the tissue mechanics simulation with growth developed by Richard Smith's group at MPI Cologne. The original program was developed within the Virtual Laboratory (VLab) modelling environment [Federl and Prusinkiewicz, 1999]. Graph structures were implemented using vertex-vertex systems integrated with CUDA (NVIDIA Corporation, Santa Clara, California,

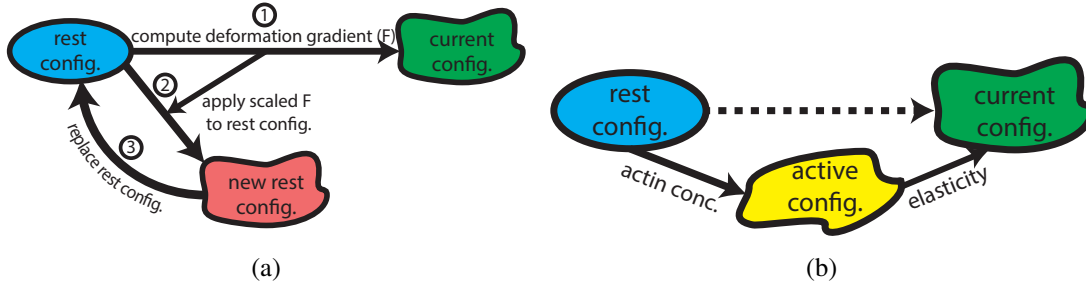


Figure 4: Implementing material relaxation and contractility using the reference configuration: 4a) Strain based relaxation is implemented replacing the rest configuration with a configuration that gradually converges towards the current configuration. 4b) Contractility is implemented assuming an active configuration exists, determined by actomyosin, which can be used to calculate elastic stresses.

U.S.) through the Thrust library [Bell and Hoberock, 2011]. The original program is thoroughly described in Gabriella Mosca’s PhD thesis [Mosca, 2016].

Our program revolves around a main time loop (Figure 5) in which the biochemistry and the mechanics are solved sequentially. For each time step, the reaction-diffusion equations governing the biochemistry are solved for a number (pdeSteps) of time steps (pdeDt), the species relevant for mechanical properties are used to update the mechanical configurations and then the mechanical equilibrium is calculated. The central time scale in the implementation is that of the reaction-diffusion equations. Non-instantaneous dynamics of active contraction and strain based relaxation are implemented as a function of the reaction-diffusion equations total time step and should occur on slower time-scales.

Simulations were run on the GPU cluster *Vesta*, managed by the Service and Support for Science IT unit (S3IT) of University of Zurich, which we greatly acknowledge.

3.5 Validation

Five analyses were run to validate our FEM program:

- Varying maxDratio (Figure 6): all measures converge as the maximal displacement ratio is decreased. We choose 0.0001 as the convergence threshold value in all simulations.
- Varying pdeSteps, keeping pdeDt constant (Figure 7): when the number of pdeSteps is low, we observe a much increased error propagation. When pdeSteps is between 5 and 20, our measures are roughly the same. We choose pdeSteps = 10.

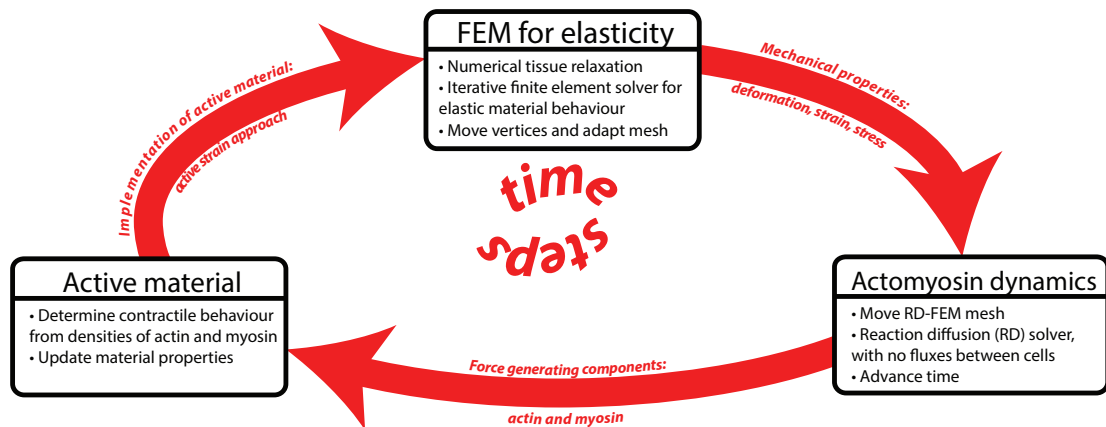
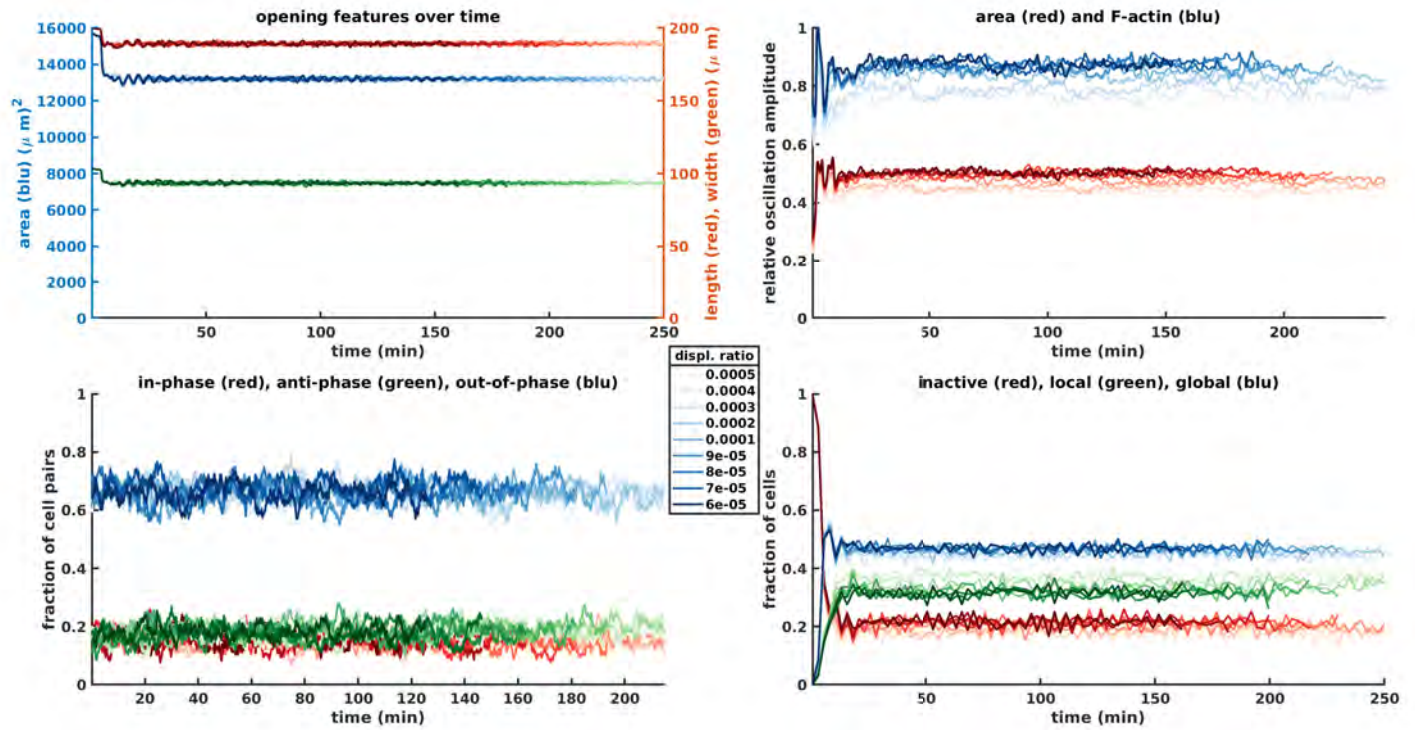


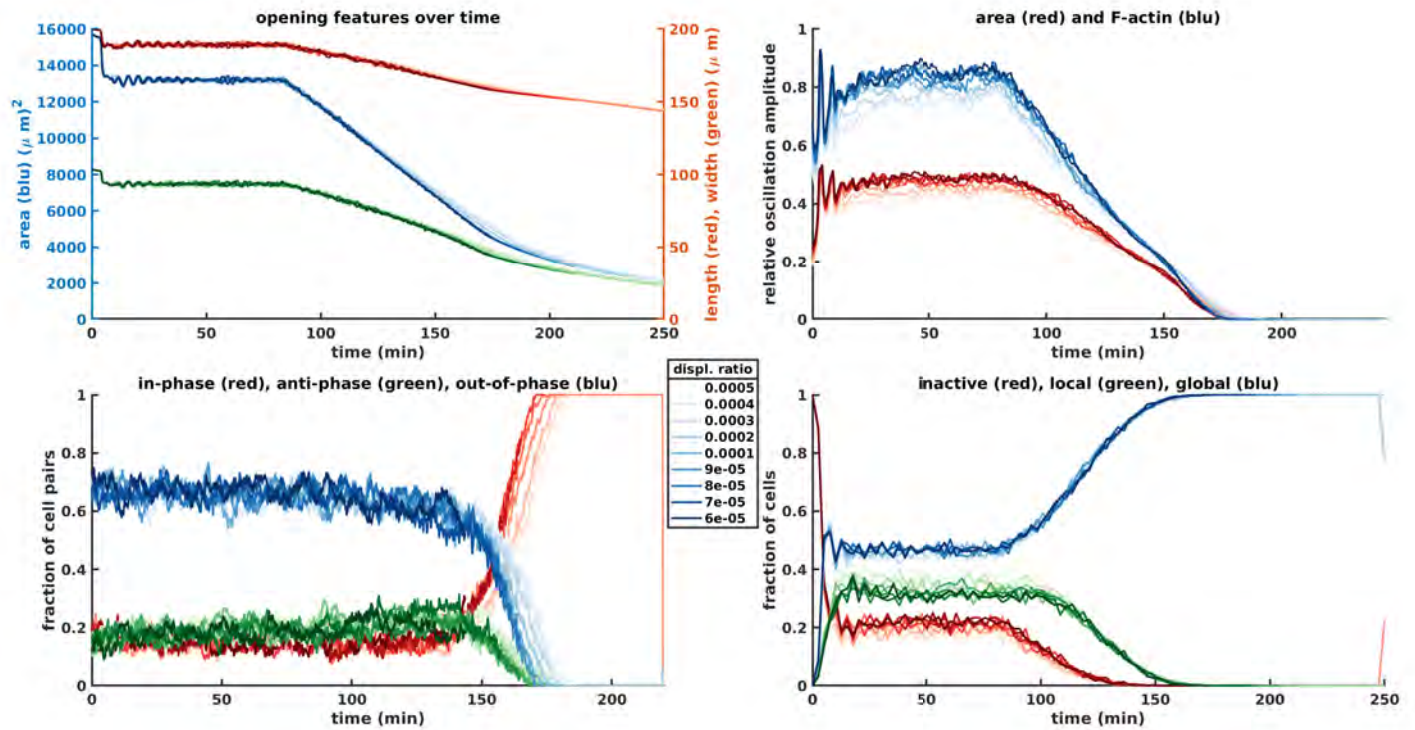
Figure 5: Diagram of mechanochemical model implementation: actomyosin dynamics, active material behaviour and elasticity-driven deformation are calculated sequentially for each step of the simulation.

- Varying $pdeDt$, keeping $pdeDt * pdeSteps$ constant (Figure 8): measures are very robust to changes in $pdeDt$. With the three largest values of $pdeDt$ that we consider, simulations diverged before the end of computational time. We set $pdeDt = 0.5$.
- A coarser and a finer mesh compared to the default mesh (Figure 9). Simulations measures do not depend on mesh resolution within the tested range.
- Multiple iterations with identical parameter values (Figure 10): simulations show good agreement over repeated runs.

Simulations in this section were carried out with parameter sets from Table 1.

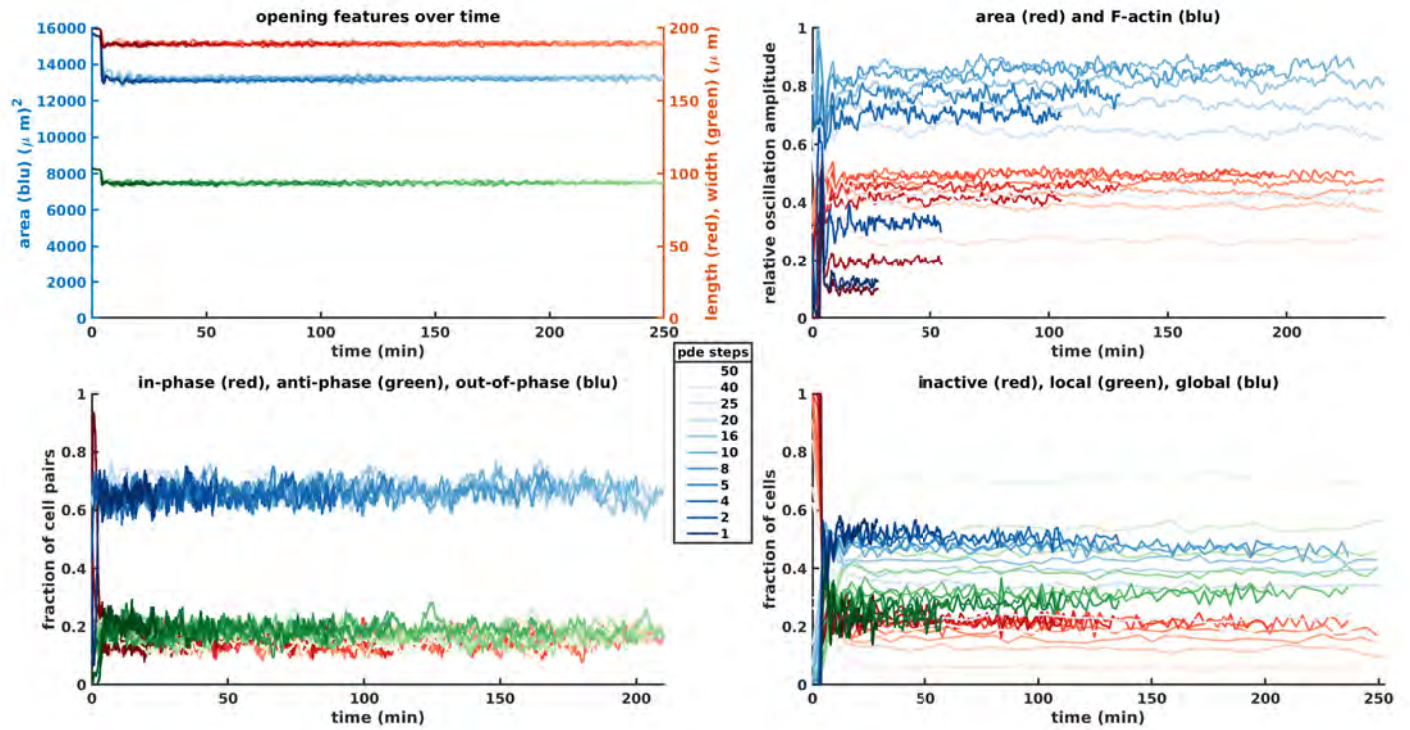


(a)

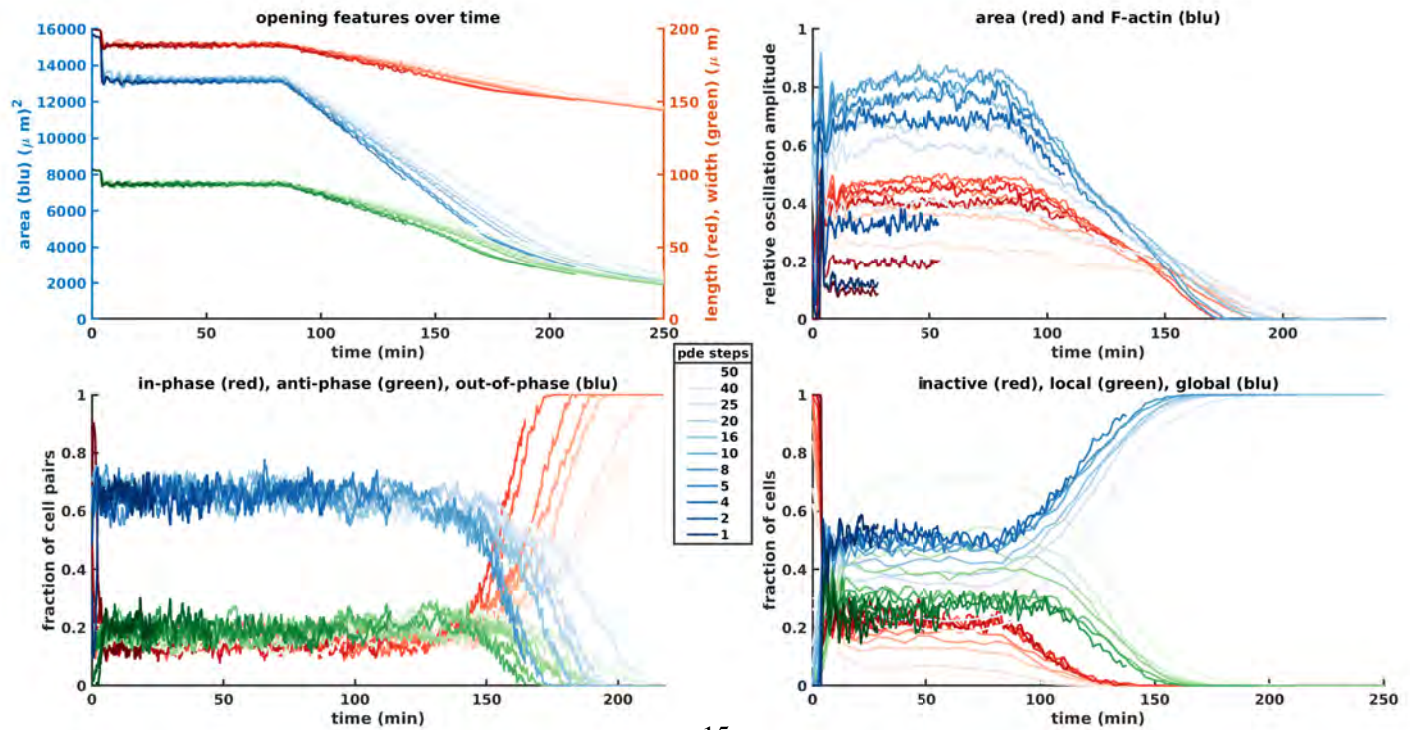


(b)

Figure 6: Opening, cellular and subcellular features as the FEM threshold displacement ratio is varied, without epidermis relaxation (6a) and with epidermis relaxation (6b).



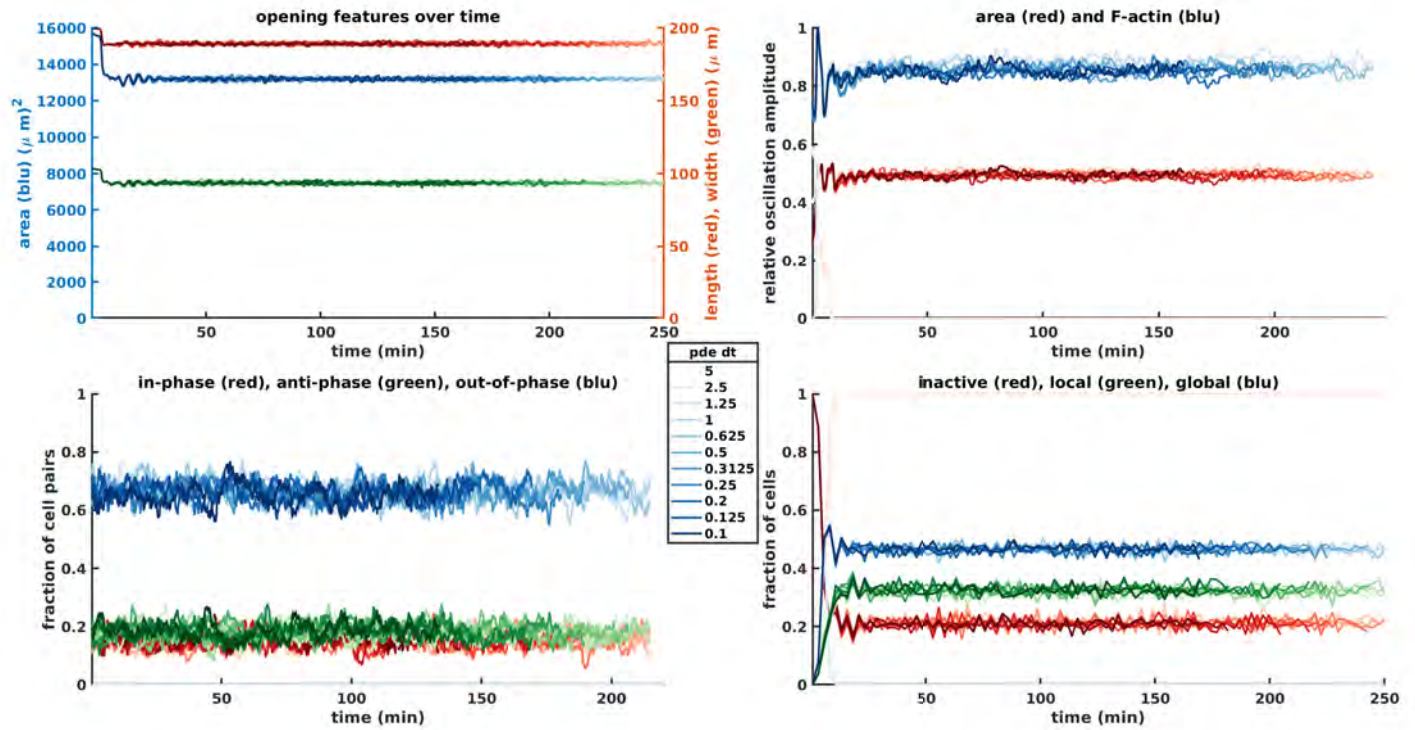
(a)



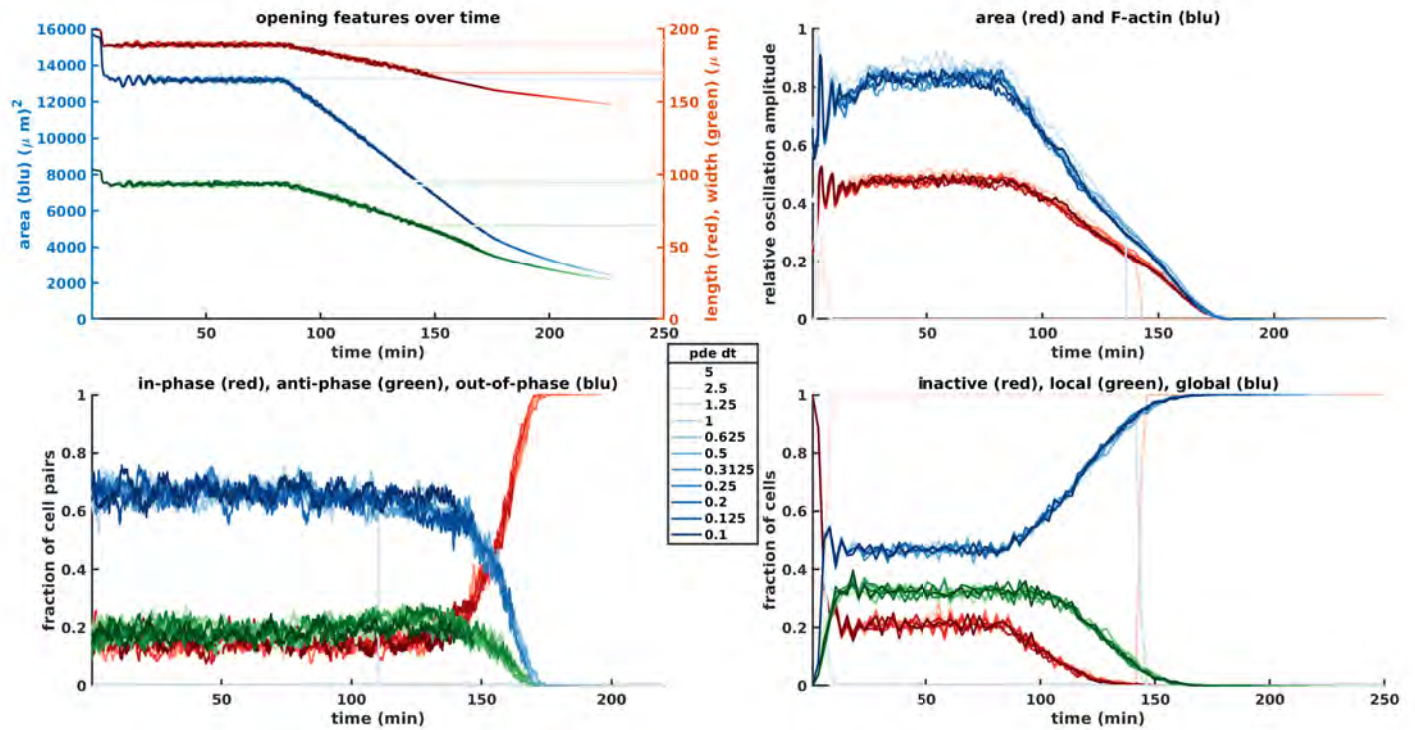
15

(b)

Figure 7: Opening, cellular and subcellular features as the number of RDE integration steps between FEM steps is varied (the time step is kept constant), without epidermis relaxation (7a) and with epidermis relaxation (7b).

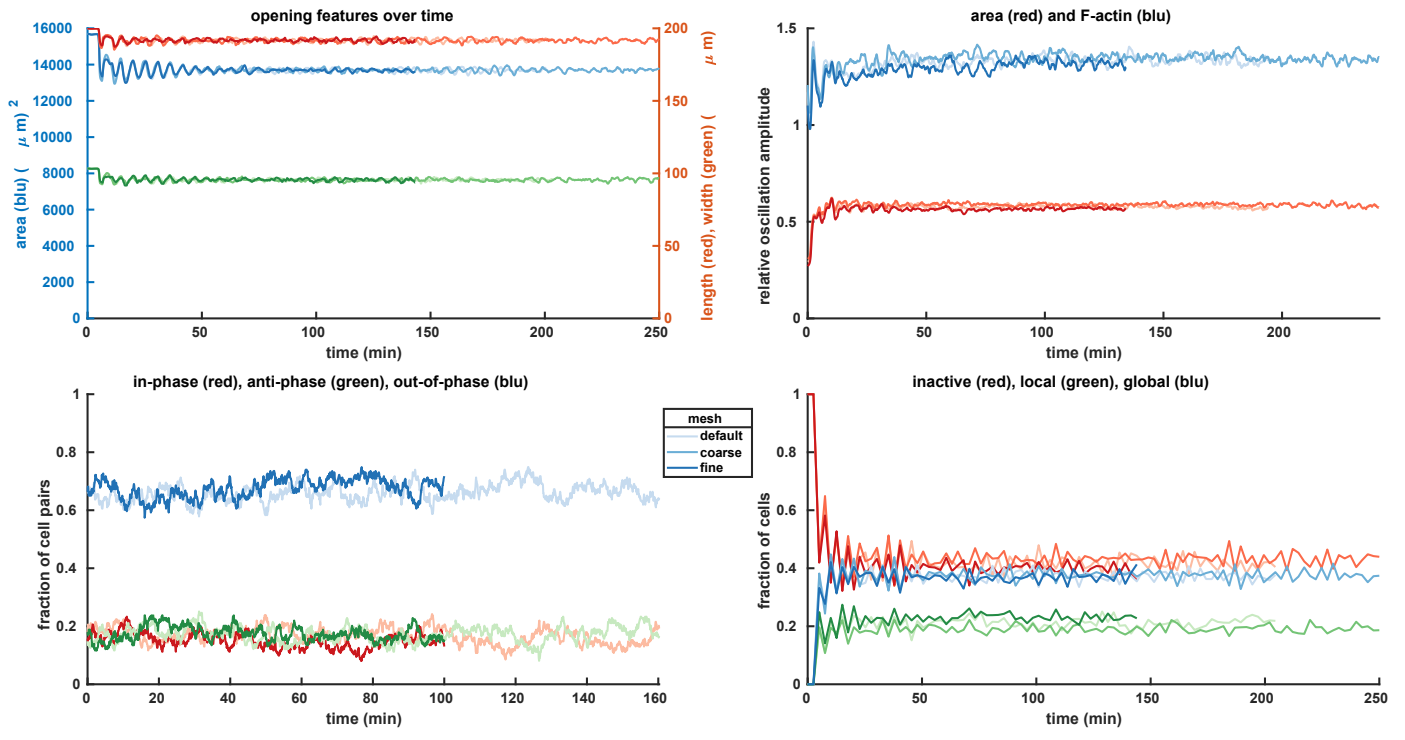


(a)

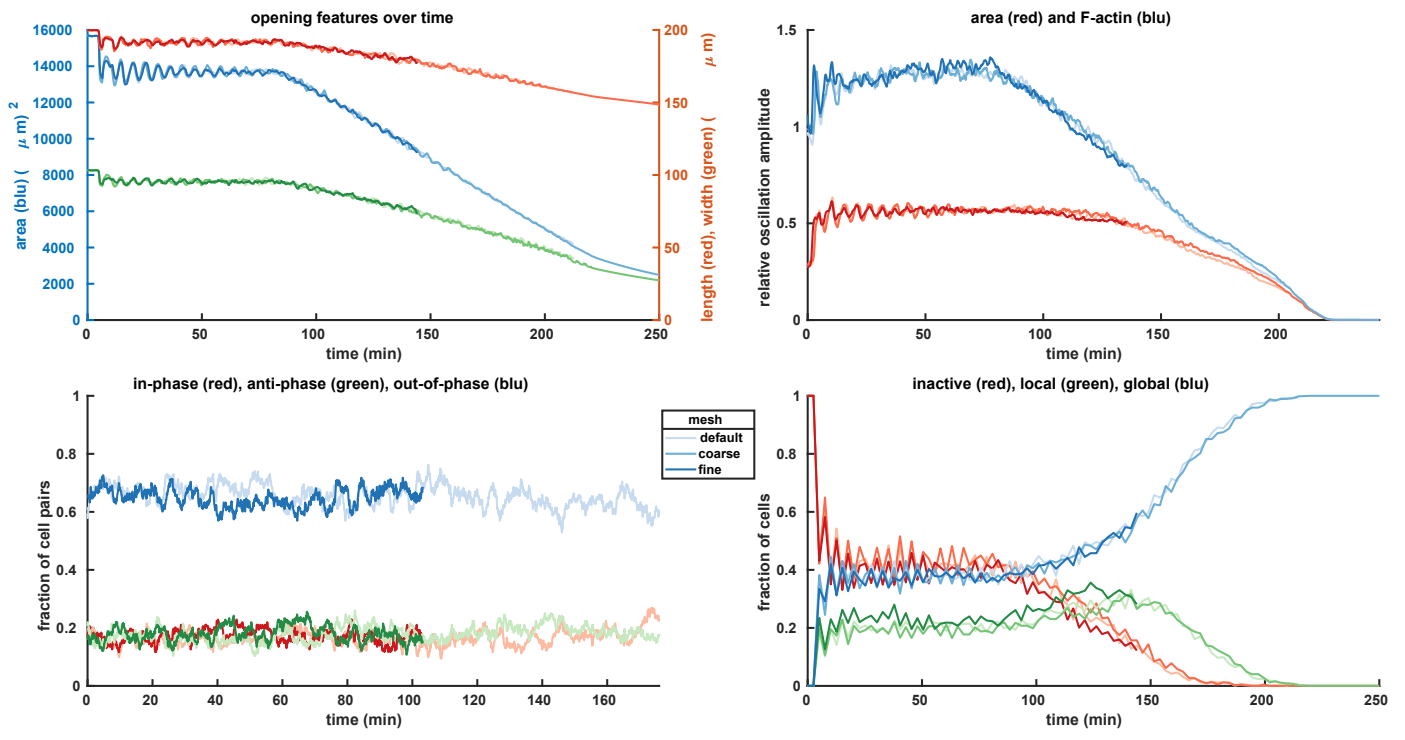


(b)

Figure 8: Opening, cellular and subcellular features as the time step of RDE integration steps is varied (the total time between FEM steps is kept constant), without epidermis relaxation (8a) and with epidermis relaxation (8b).

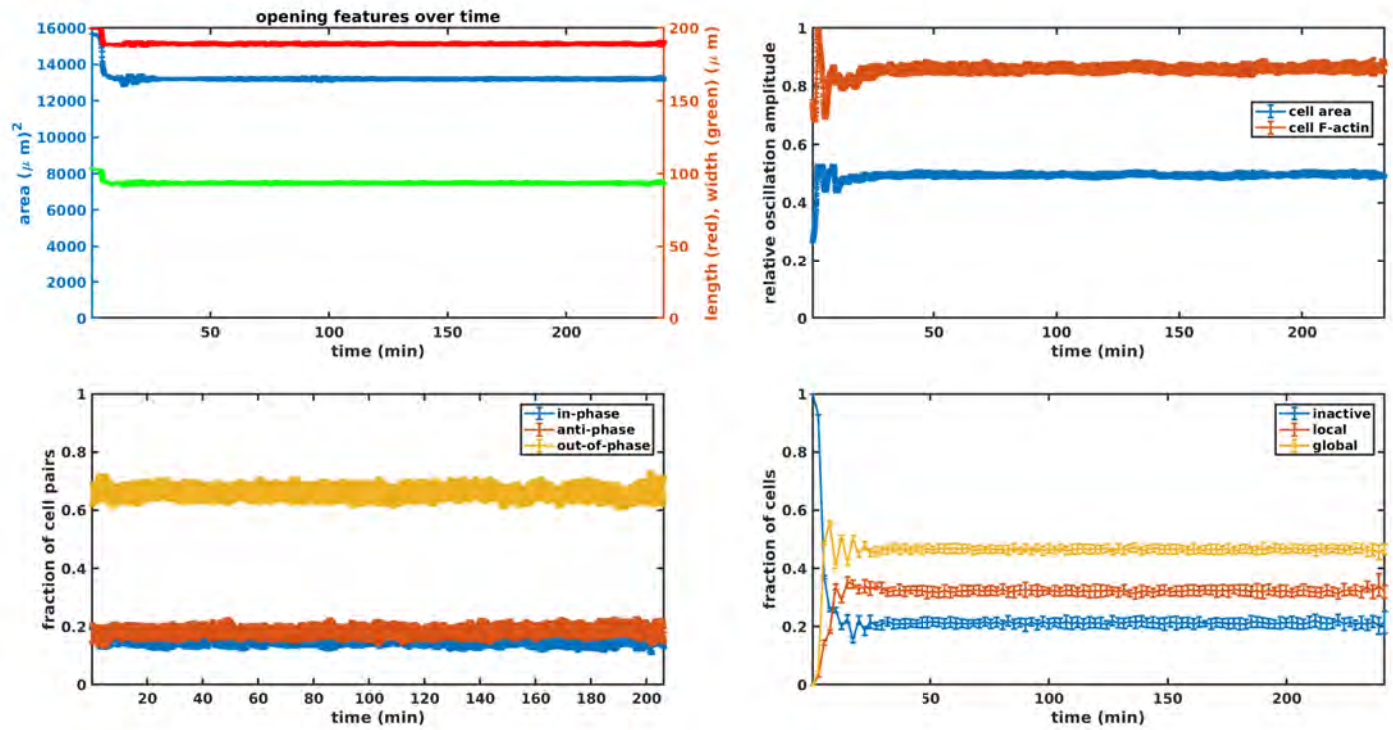


(a)

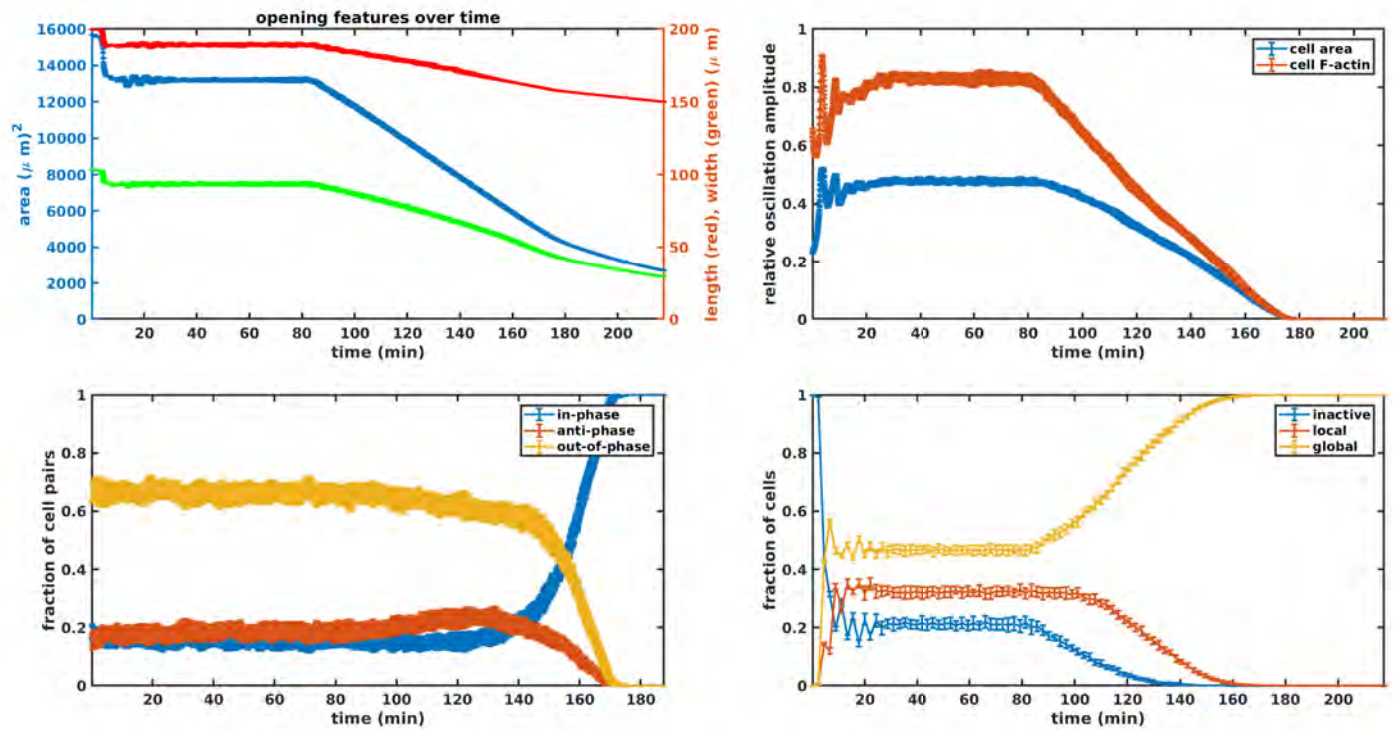


(b)

Figure 9: Opening, cellular and subcellular features as the mesh resolution is varied, without epidermis relaxation (9a) and with epidermis relaxation (9b). Coarse, default and fine meshes have 8895, 15782 and 26055 mechanical finite elements, respectively. Opening areas very closely overlap, so only the top curve is visible. Phase correlations were not calculated for the coarse mesh due to a bug in the boundary elements classification (comparison between default and fine is more important anyway).



(a)



(b)

Figure 10: Average and standard deviation of opening, cellular and subcellular features in multiple iterations of “Optimal arrest scenario” (see Table 1), without epidermis relaxation (10a) and with epidermis relaxation (10b).

4 Methods

4.1 Analytical methods for parameter spaces

Qualitative behaviour of equations during reaction-diffusion system development was calculated with linear stability analysis [Murray, 2003] using MATLAB's symbolic computation toolbox. We considered reaction-diffusion equations in their generalised form

$$\frac{\partial \mathbf{x}}{\partial t} = \mathbf{F}(\mathbf{x}) + D\Delta \mathbf{x},$$

where \mathbf{x} , \mathbf{F} denote the vectors of concentration values and reaction functions, respectively, with x_i and F_i their elements, and D is the diagonal matrix of diffusion coefficients. Then, the Jacobian matrix at a steady state \mathbf{x}^* s.t. $\mathbf{F}(\mathbf{x}^*) = 0$ is defined as

$$\mathbf{J}(\mathbf{x}^*) = \left[\begin{array}{ccc} \frac{\partial f_1}{\partial x_1} & \cdots & \frac{\partial f_1}{\partial x_n} \\ \vdots & \ddots & \vdots \\ \frac{\partial f_m}{\partial x_1} & \cdots & \frac{\partial f_m}{\partial x_n} \end{array} \right] \Bigg|_{\mathbf{x} = \mathbf{x}^*}$$

We defined the \mathbf{F} of each system symbolically in MATLAB and used the function *jacobian* to calculate $\mathbf{J}(\mathbf{x}^*)$ as a function of equation parameters. Then, the eigenvalues λ of $\mathbf{J}(\mathbf{x}^*)$ were used to determine whether the steady state in the absence of diffusion was oscillatory in a given parameter choice as follows:

- for two-dimensional systems, oscillating solutions satisfy $\det(\mathbf{J}) > 0$ and $\text{trace}(\mathbf{J}) > 0$.
- for three-dimensional systems, oscillating solutions satisfy $\text{real}(\lambda_1) < 0$, $\text{real}(\lambda_2 \text{ and } 3) > 0$ and $\text{imag}(\lambda_2) = -\text{imag}(\lambda_3) > 0^1$.

When diffusion is included, we calculated the eigenvalues $\lambda(k)$ of $Dk^2 - \mathbf{J}$, with k the wave-number. Then, spatial patterns spontaneously emerge at a steady state of the diffusion-free system if $\max(i, k)(\lambda_i(k)) > 0$, with the preferred wave length being $\frac{2\pi}{k^*}$, and $k^* = \text{argmax}_k(\lambda_i(k))$.

Defining \mathbf{F} is straightforward in all cases except for Equation 5. There, we considered the diffusion free-case, which leads to space-independent concentration-values and use the contractility function Equation 7 evaluated at steady state to replace the cell area dependency of $\frac{S_0}{S_t}$. Hence, F_1

¹*eig* returns eigenvalues always in the same order.

evaluated at the steady state given by $F = \alpha + \beta$ reads

$$\gamma \left(\beta \left(1 + \frac{\text{cMax}}{1 + (\text{cFthr}/(\alpha + \beta))^n} \right)^2 - \Phi \right),$$

where parameters are defined as in Equation 5 and Equation 7. F_2 and F_3 are unchanged.

4.2 Mesh generation

The input mesh is generated starting from the maximum projection of a 3D light sheet microscopy image. We chose an image acquired at the time when the canthi form (Figure 11a). On this image, the AS cells were manually segmented, using a custom made MATLAB program (Figure 11c). Only the points of intersection of 3 or more cells were marked, making the cell edges straight in our geometry. The ES material is modelled as a continuum so we do not segment ES cells. Once AS cells are segmented, the entire AS tissue is meshed into triangular finite elements using a routine based on distmesh [Persson and Strang, 2004] (Figure 11e). We further constrain the mesh generator to get polygons with straight edges by adding additional fixed points on the cell edges (Figure 11d). Around the AS tissue, we then define a region of ES that is explicitly included in the simulations and mesh that too (Figure 11f). The meshes are conforming between AS cells as well as between ES and AS.

Once the first layer of finite elements is defined, the mesh is exported to a text file and read into our C++ program, which takes care of the finer meshing for solving RDEs.

4.3 Measures of simulated phenotypes

- **relative oscillation amplitude** of a cell area $a(t)$ at time t' is defined as $\frac{\max(a(t)) - \min(a(t))}{2 * \text{mean}(a(t))}$, with $t \in [t' - w, t' + w]$ and w chosen as approximately 1.5-time the oscillation period.
- **neighbouring cell oscillations phase shift** is calculated as the time shift of average F-actin signals in the triangles on the two sides of the cell boundary between two cells. The time shift is calculated for moving time windows of approximately 1.5 times the oscillation period of length. The shift is calculated in radians using an algorithm based on the discrete Fourier transform (adapted from [Zhimirov, 2016]). The algorithm defines the shift between the two signals as the difference in phase between the components of each signal with the largest signal. The shift is then mapped onto the interval $[0, \pi]$. In-phase, respectively anti-phase oscillating cell pairs are defined to be those whose shift is within $\pi/6$ of 0, respectively π .

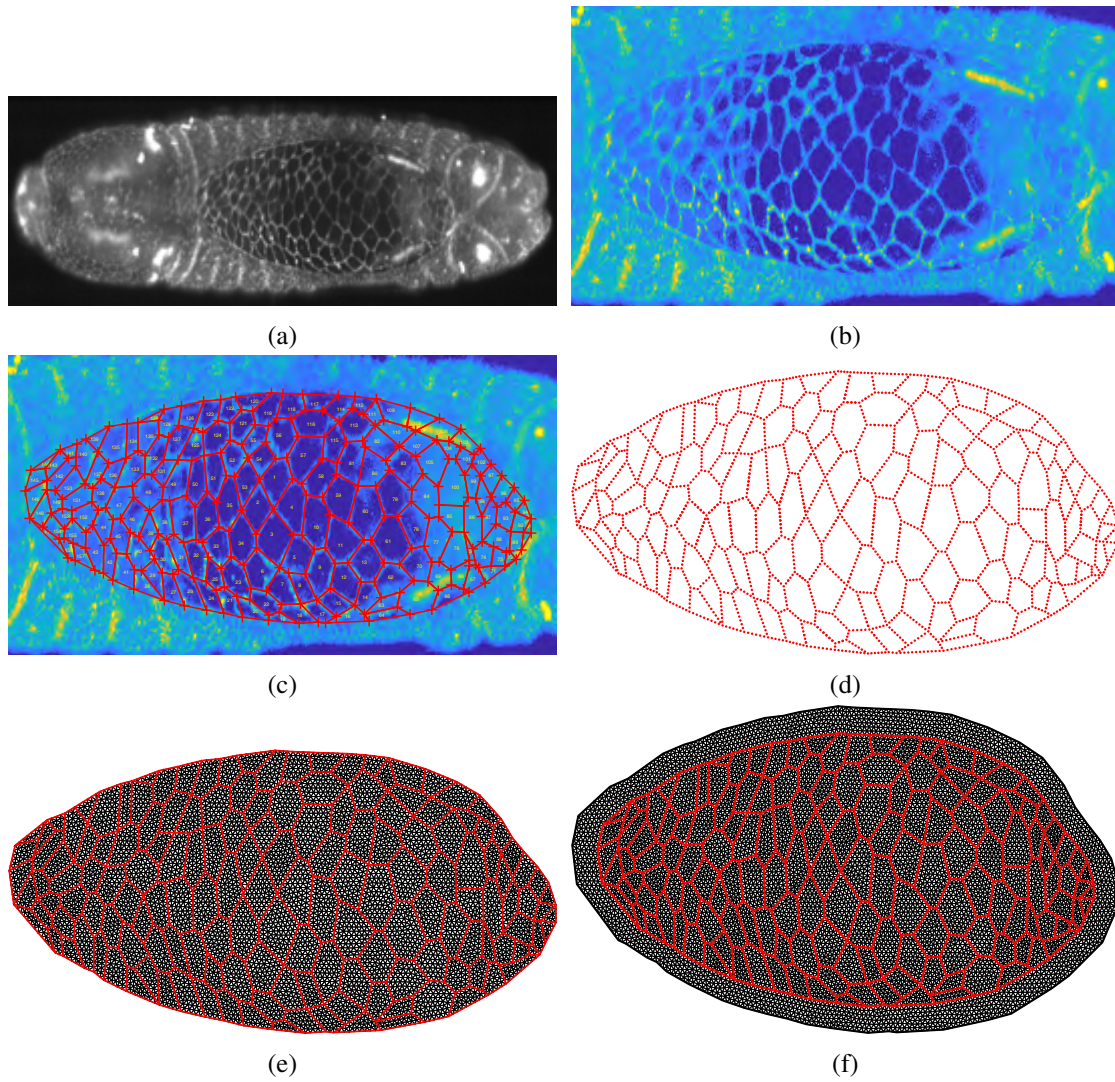


Figure 11: Mesh generation pipeline: 11a) choose frame of dorsal closure just before canthi formation (image by David Dreher) 11b) Load image into the polyGui 11c) manually segment cells 11d) impose equally spaced, fixed vertices to pass to 2D mesh generator 11e) mesh amnioserosa with triangular elements 11f) add epidermal mesh around amnioserosa.

All other values are considered to be out-of-phase. The values in 2D parameter spaces are averaged over cells and time.

- **passive, locally active and globally active cells.** Let f be the fraction of reference area of the cell with F-actin concentration over a threshold value of 1.3. Then passive cells have $f < 0.2$, locally active cells have $0.2 < f < 0.6$ and globally active cells have $f > 0.6$. Thresholds are chosen so that the classification is not too sensitive to their exact value. The values in 2D parameter spaces are averaged over cells and time.
- **arrest time** is defined as the last time a cell has less than 0.9 of its reference area covered by F-actin.

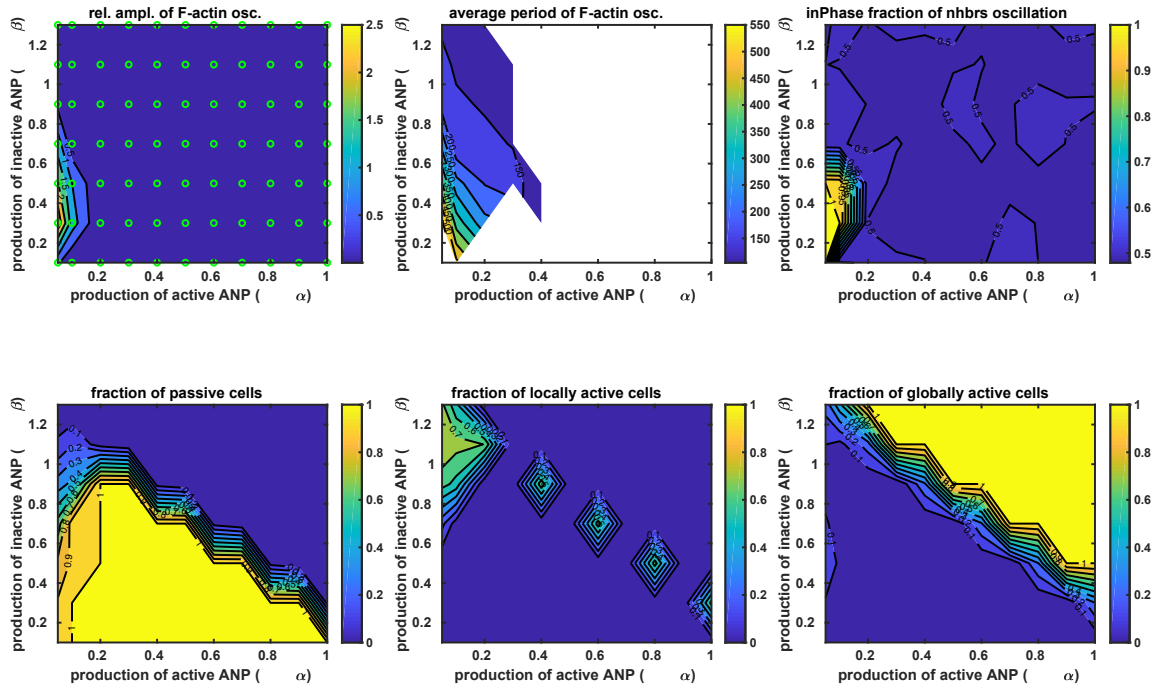


Figure 12: Large parameter screen varying production rates of ANPi and ANPa, with no contractility.

5 Results

In the main text simulations reproducing F-actin oscillations in absence of Myosin II contractility were shown. Since analytical methods were used to determine the region of parameter space leading to oscillations, the exploration of parameter space was initially limited to a small region. Here, Figure 12 shows the effect of varying the production rates of ANPi and ANPa in the same region of parameter space as in the scenario with mechanical contractility (main text figures). Comparing the two figures shows that the spatial features of F-actin dynamics (bottom row) are similar in the two scenarios. In contrast, oscillation features are modulated by the presence of Myosin II, with some parameter values exhibiting oscillations only when Myosin II is added to the simulations.

Not only Myosin II determines whether oscillations emerge, but also the amplitude and period of oscillations. In our simulations, Myosin II generally increases the period of oscillations. This is in contrast to preliminary experimental data by L. Pasakarnis [Pasakarnis, 2016], so we wondered whether any parameter of our reaction-diffusion system would modulate the effect of Myosin II

on the oscillation period. Prime candidates were F_t , the threshold F -concentration for negative feedback of F-actin onto ANPi activation and γ , the parameter regulation the rate of reactions, independently of diffusion coefficients. Figure 13 shows no dramatic changes in F_t and γ , but still indicates that reducing F_t reduces the difference between average periods until nearly 0. It remains to be verified whether the effect of varying F_t is robust across parameter space.

When considering the rate of closure progression, it is worth noting that this is influenced both by the relaxation rate of the epidermis and by the parameters of the reaction-diffusion and force-generation mechanisms. For example, increasing the maximal contractility or increasing the production rate of ANPi (β) lead to smaller amnioserosa tissue areas, both before relaxation begins and as dorsal closure progresses (Figure 14). *In vivo* this would be reflected in amnioserosa tissue area being influenced by F-actin nucleators and Myosin II activity. Actomyosin perturbation experiments, such as the formin Diaphanous over-expression experiment, or the expression of Myosin II kinase [Fischer et al., 2014] support the model prediction. *In vivo*, though, it is not trivial to decouple the effect of amnioserosa specific genetic perturbation to that of epidermis material behaviour.

During dorsal closure progression, cell areas oscillations arrest in a sequential fashion, from the outer to the inner-most amnioserosa cells. Even before the onset of dorsal closure, amnioserosa cells exhibit an apical surface gradient whereby the outer-most cells are the smallest and the inner-most the largest. Thereby, the sequential oscillations arrest could be a consequence of the cells geometry. To rule out this hypothesis an artificial segmentation of the amnioserosa tissue was designed in which all cells have a near-identical surface area. In this scenario, the oscillations dependence on parameter values (Figure 20) and the patterns of sequential pulsation arrest (Figure 15) remain largely unchanged compared to the image-based amnioserosa cells segmentation.

The pattern of sequential oscillations arrest depends on amnioserosa cells properties and also on the mechanical and geometrical features of the surrounding epidermis tissue. In the main text, the effect of varying epidermis height and Young's modulus was considered. Here, in Figure 16, the effect of varying the epidermis width and Young's modulus is examined. The results on width and height of the epidermis are consistent with each other and support the prediction of sequential oscillations arrest proceeding along the axis where the epidermis tissue is more easily elongated.

5.1 Additional parameter screens

Since the production rates of ANPi and ANPa, respectively α and β , are crucial system parameters, the following additional screens were run to confirm that their behaviour is conserved across

variations of the values of parameters that have so-far not been explored:

- $\alpha - \beta$ for $\tau = 0.25, 0.75$ (Figure 17)
- $\alpha - \beta$ for $A_t = 5, 10$ (Figure 18)
- $\alpha - \beta$ for $F_t = 0.7, 1.3$ (Figure 19)

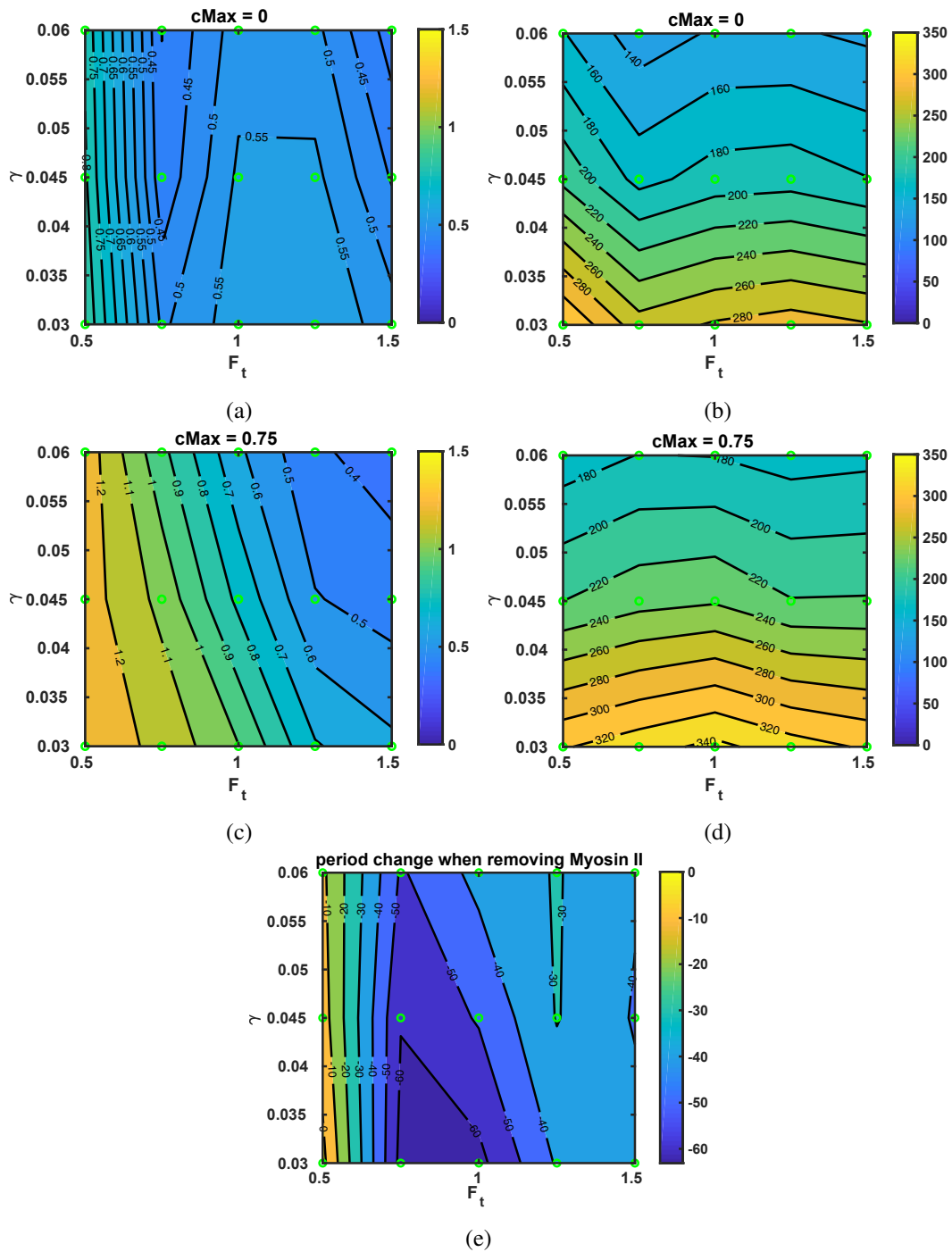


Figure 13: Modulating the difference in period between simulations corresponding to Myosin II mutant and wild type: 13a,13c) average relative amplitude of F-actin oscillation. 13b,13d) average period (seconds) of F-actin oscillation. 13b) period without Myosin II minus period with Myosin II (in seconds).

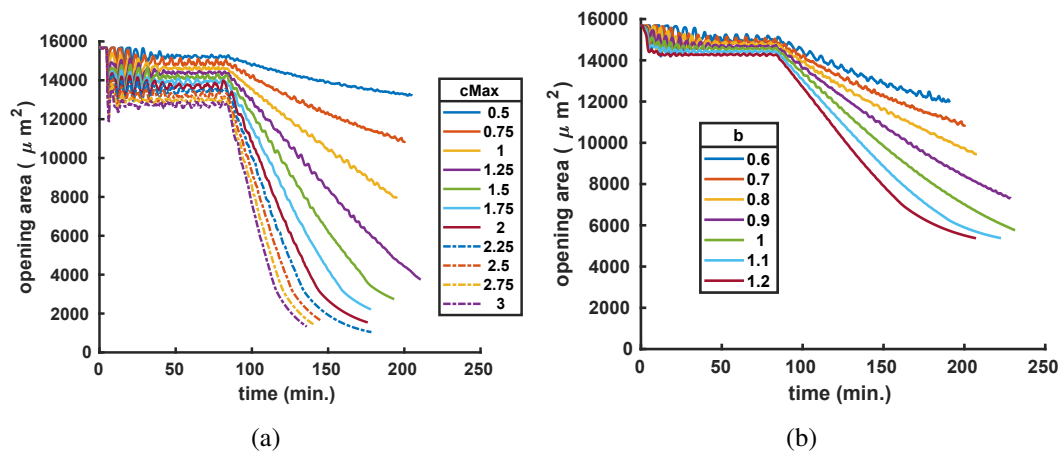


Figure 14: Opening area as c_{Max} (14a) or β (14b) are changed.

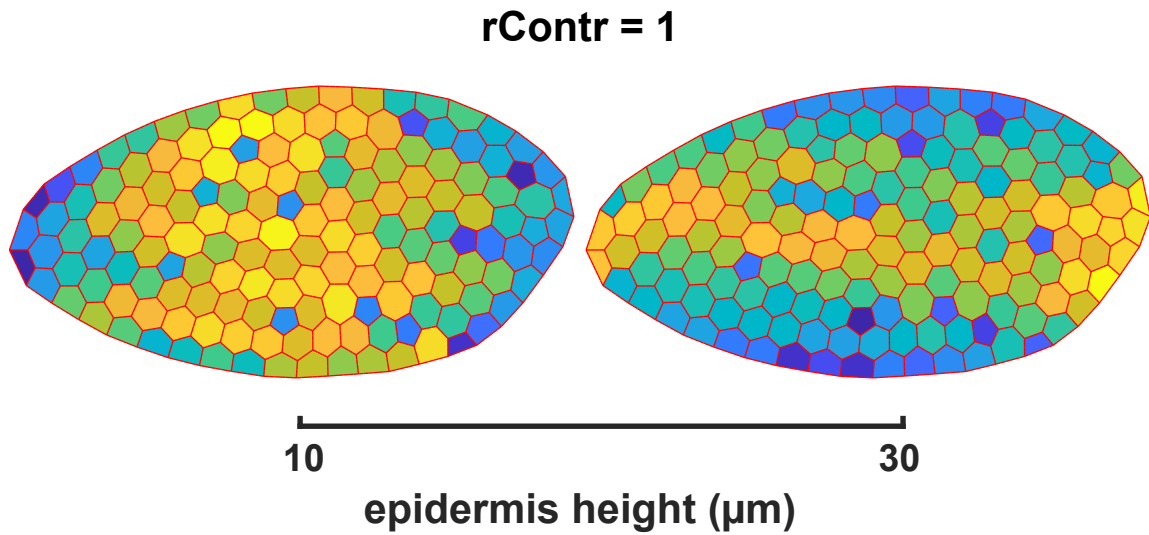


Figure 15: Sequential pulsation arrest in computer-generated amnioserosa tissue with equal cells

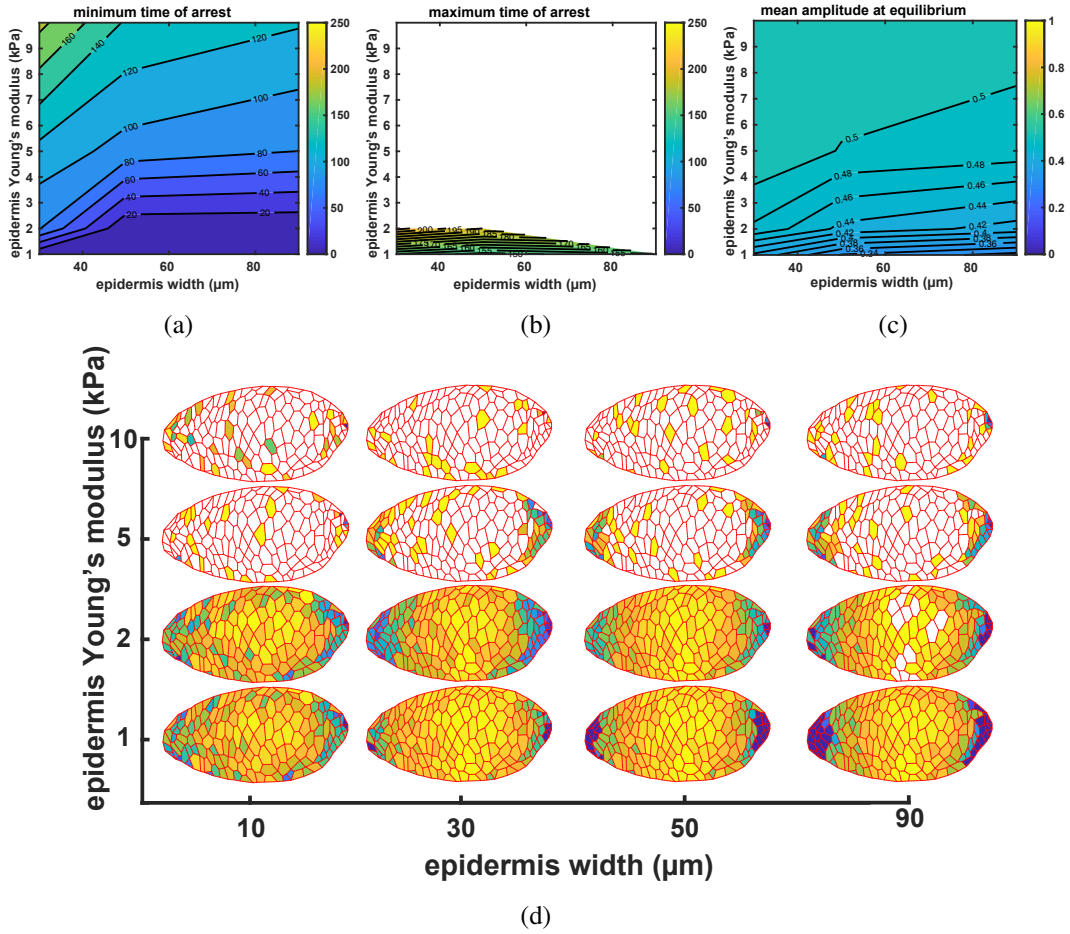
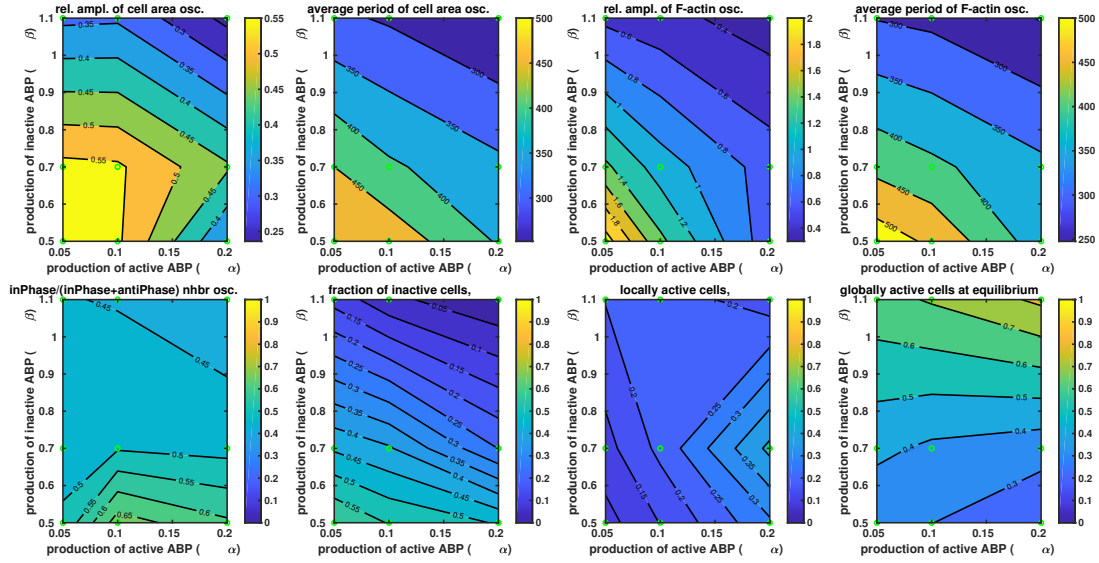
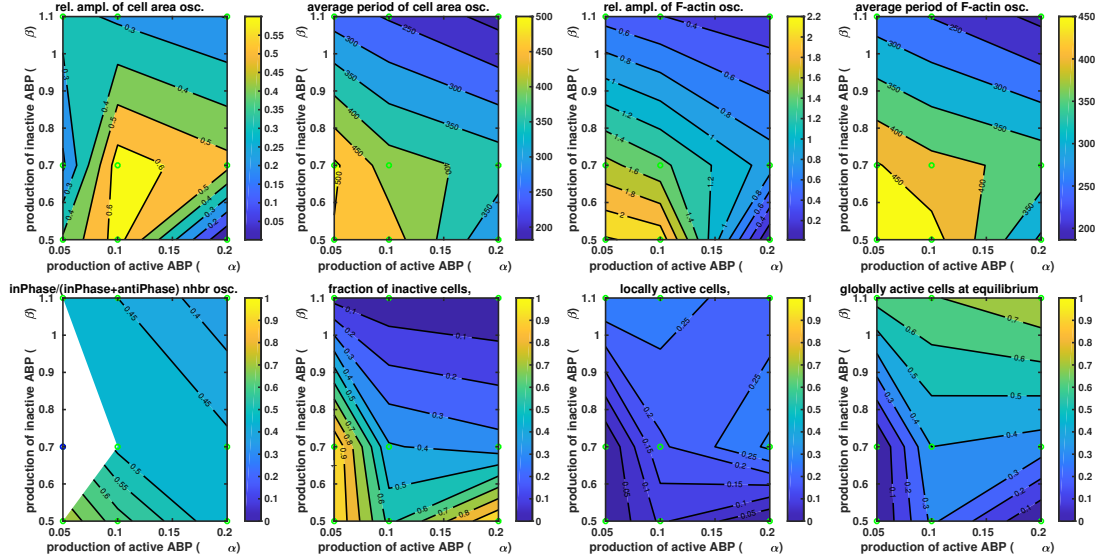


Figure 16: Varying epidermis size and Young's modulus modulates the spatial pattern of pulsation arrest: top) minimum and maximal time of cell area oscillation arrest, and mean relative amplitude of oscillations in the early stages of dorsal closure. White regions, if any in plot of minimum, respectively maximum time of arrest, correspond to no, respectively not all cells arresting. bottom) cells coloured according to their time of oscillation arrest. The minimum and maximum of arrest define the colour-scale limits of each opening.

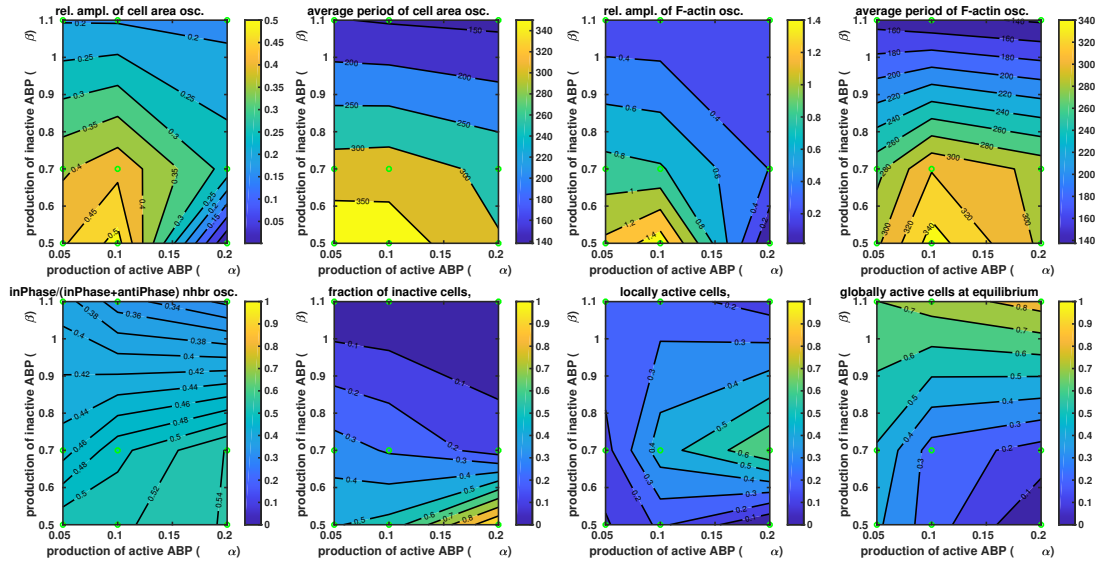


(a) $r_1 = 0.25$

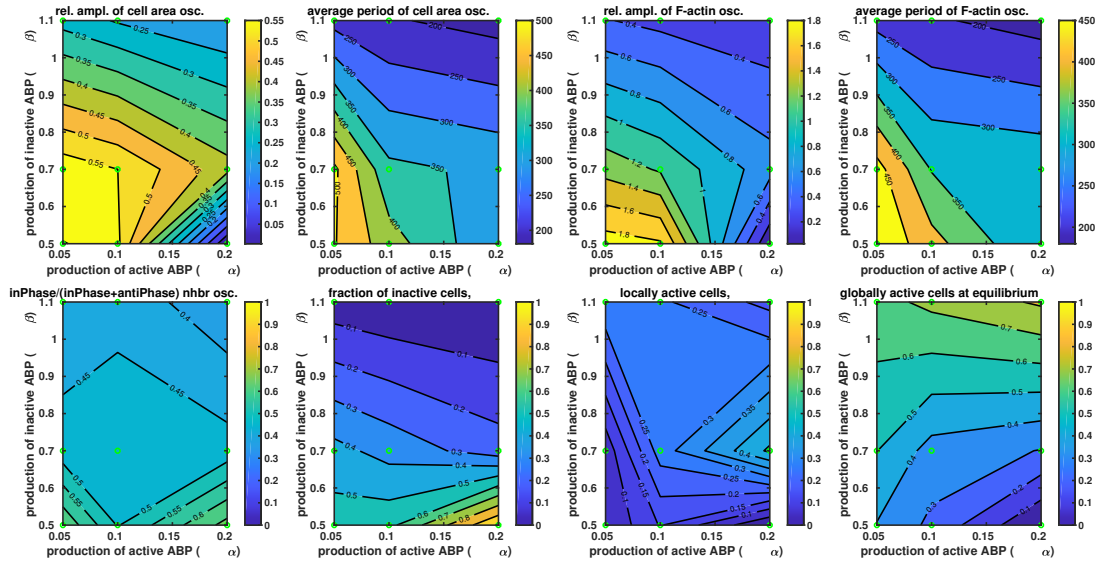


(b) $r_1 = 0.75$

Figure 17: $\alpha - \beta$ screen as r_1 is varied.

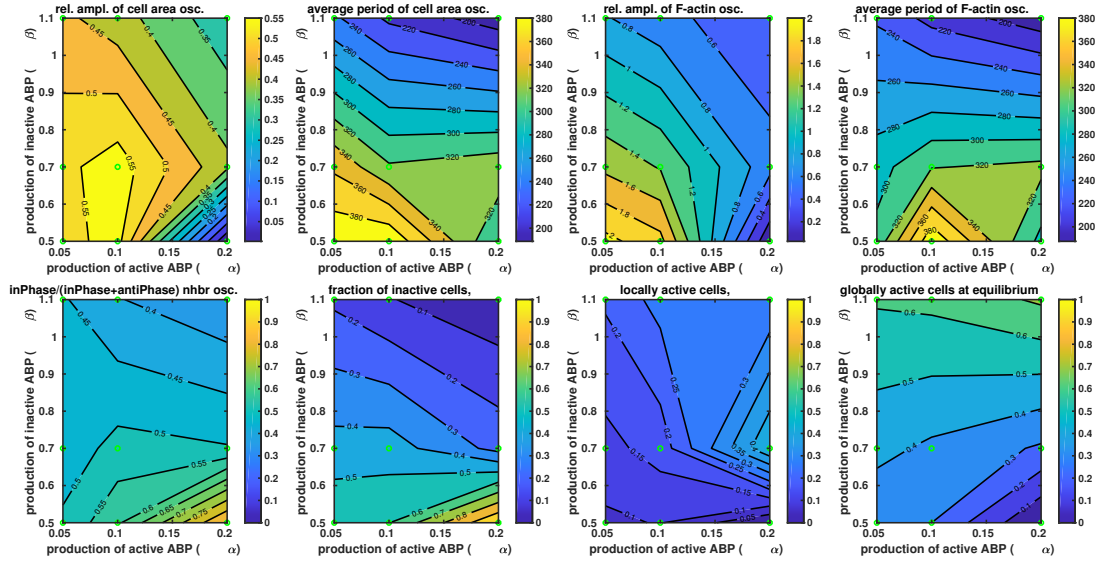


(a) $A_t = 5$

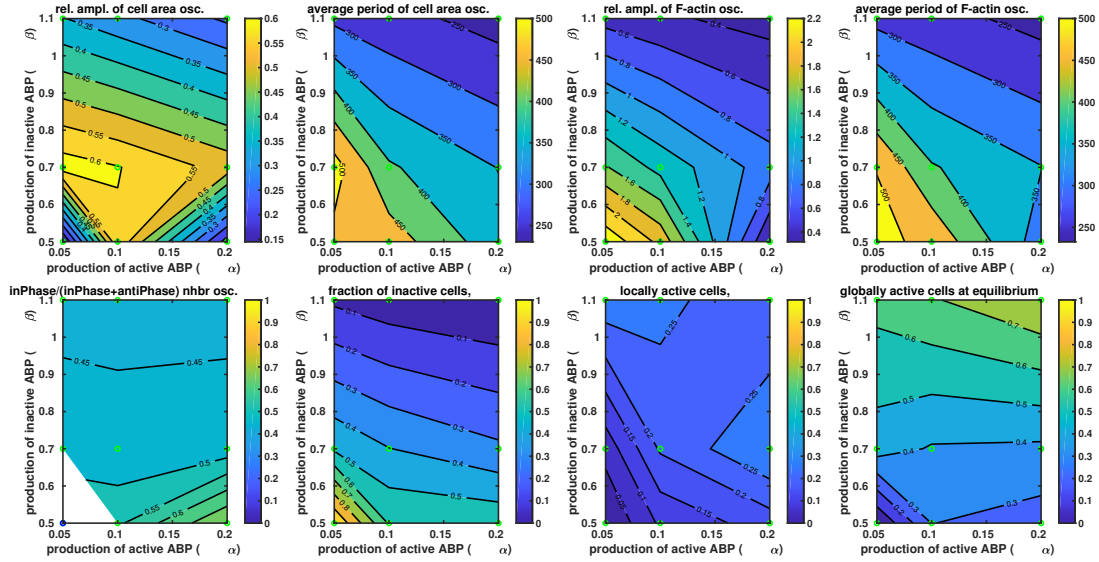


(b) $A_t = 10$

Figure 18: $\alpha - \beta$ screen as A_t is varied.



(a) $F_t = 0.7$



(b) $F_t = 1.3$

Figure 19: $\alpha - \beta$ screen as F_t is varied.

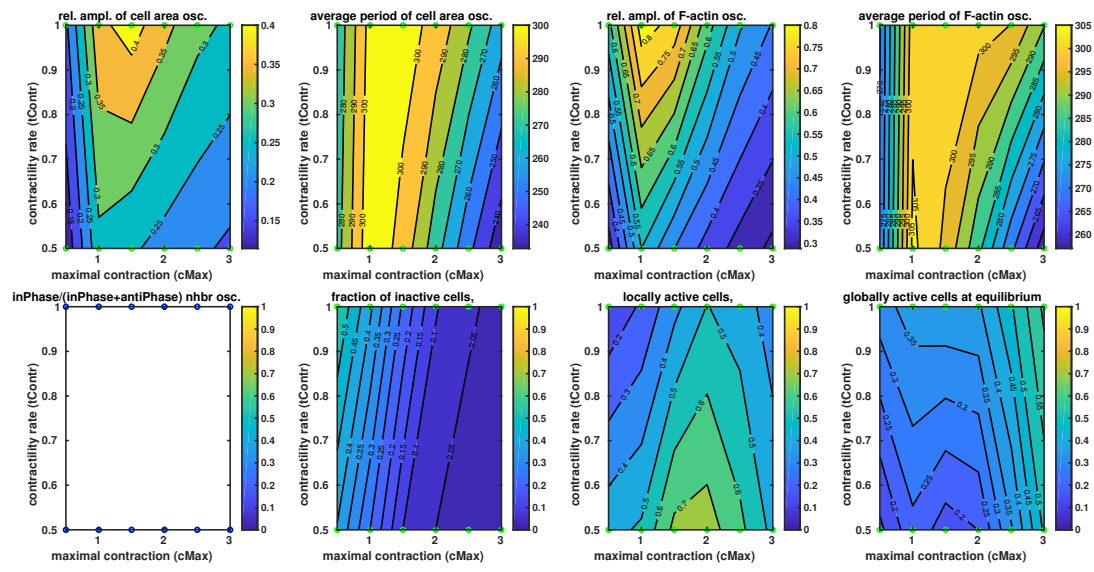


Figure 20: cMax and rContr with equal cells geometry

5.2 Parameter values

Scenario	<i>No mech.</i> ^a	<i>No relax.</i> ^b	<i>Relax.</i> ^c	<i>Optimal arrest</i> ^d
Reaction-diffusion (eq. 5)				
D_I	10	10	10	10
D_A	0.1	0.1	0.1	0.1
D_F	0.001	0.001	0.001	0.001
α	0.05	0.1	0.1	0.1
β	0.8	0.7	0.7	0.9
γ	0.03	0.045	0.045	0.045
A_t	15	15	15	15
F_t	1	1	1	1
r_1	0.5	0.5	0.5	0.5
Active material (eq. 7)				
cMax	0	0.75	0.75	2
cFthr	ND	1.5	1.5	1.5
n	ND	6	6	6
Mechanics				
rel. timescale	ND	∞	15 <i>min</i>	40 <i>min</i>
ES- E	ND	1 <i>kPa</i>	1 <i>kPa</i>	1 <i>kPa</i>
ES- ν	ND	0.45	0.45	0.45
Geometry				
ES-height	ND	10 μm	10 μm	10 μm
ES-width	ND	10 μm	10 μm	10 μm

Table 1: Parameters of figures with Turing patterning model. Scenarios correspond to: *No mech.*, myosin mutant; *No relax.*, early stage oscillations; *Relax.*, closure progression; *Optimal arrest*, accelerated closure for more cells to arrest. Closure is speeded up to optimise closure duration with respect to computing time. ^a) Fig. 2D-2F. ^b) Fig. 3, 6. ^c) Fig. 5A. ^d) Fig. 4B-D, 5B-D.

References

- [Almeida et al., 2011] Almeida, L., Bagnerini, P., Habbal, A., Noselli, S., and Serman, F. (2011). A mathematical model for dorsal closure. *Journal of theoretical biology*, 268(1):105–119.
- [Ambrosi and Pezzuto, 2012] Ambrosi, D. and Pezzuto, S. (2012). Active stress vs. active strain in mechanobiology: Constitutive issues. *Journal of Elasticity*, 107(2):199–212.

- [Arcuri and Murray, 1986] Arcuri, P. and Murray, J. D. (1986). Pattern sensitivity to boundary and initial conditions in reaction-diffusion models. *Journal of Mathematical Biology*, 24(2):141–165.
- [Aristotelous et al., 2018] Aristotelous, A., Crawford, J., Edwards, G., Kiehart, D., and Venakides, S. (2018). Mathematical models of dorsal closure. *Progress in Biophysics and Molecular Biology*, pages –.
- [Barreira et al., 2011] Barreira, R., Elliott, C. M., and Madzvamuse, A. (2011). The surface finite element method for pattern formation on evolving biological surfaces. *Journal of Mathematical Biology*, 63(6):1095–1119.
- [Bassel et al., 2014] Bassel, G. W., Stamm, P., Mosca, G., Barbier de Reuille, P., Gibbs, D. J., Winter, R., Janka, A., Holdsworth, M. J., and Smith, R. S. (2014). Mechanical constraints imposed by 3D cellular geometry and arrangement modulate growth patterns in the Arabidopsis embryo. *Proceedings of the National Academy of Sciences of the United States of America*, 111(23):8685–90.
- [Bell and Hoberock, 2011] Bell, N. and Hoberock, J. (2011). Thrust: A productivity-oriented library for cuda. In *GPU computing gems Jade edition*, pages 359–371. Elsevier.
- [Brinkmann et al., 2018] Brinkmann, F., Mercker, M., Richter, T., and Marciniak-Czochra, A. (2018). Post-turing tissue pattern formation: Advent of mechanochemistry. *PLOS Computational Biology*, 14(7):1–21.
- [Brodland and Clausi, 1994] Brodland, G. and Clausi, D. (1994). Embryonic tissue morphogenesis modeled by fem. *Journal of biomechanical engineering*, 116(2):146–155.
- [Brodland and Veldhuis, 2012] Brodland, G. W. and Veldhuis, J. H. (2012). The Mechanics of Metastasis: Insights from a Computational Model. *PLoS ONE*, 7(9):e44281.
- [Cherubini et al., 2008] Cherubini, C., Filippi, S., Nardinocchi, P., and Teresi, L. (2008). An electromechanical model of cardiac tissue: Constitutive issues and electrophysiological effects. *Progress in Biophysics and Molecular Biology*, 97(2-3):562–573.
- [Davidson et al., 1995] Davidson, L., Koehl, M., Keller, R., and Oster, G. (1995). How do sea urchins invaginate? using biomechanics to distinguish between mechanisms of primary invagination. *Development*, 121(7):2005–2018.

- [Dierkes et al., 2014] Dierkes, K., Sumi, A., Solon, J., and Salbreux, G. (2014). Spontaneous Oscillations of Elastic Contractile Materials with Turnover. *Physical Review Letters*, 113(14):148102.
- [Dziuk and Elliott, 2007] Dziuk, G. and Elliott, C. M. (2007). Finite elements on evolving surfaces. *IMA Journal of Numerical Analysis*, 27(2):262–292.
- [Elliott et al., 2012] Elliott, C. M., Stinner, B., and Venkataraman, C. (2012). Modelling cell motility and chemotaxis with evolving surface finite elements. *Journal of the Royal Society Interface*, 9(June):3027–3044.
- [Federl and Prusinkiewicz, 1999] Federl, P. and Prusinkiewicz, P. (1999). Virtual laboratory: an interactive software environment for computer graphics. *Proceedings Computer Graphics International CGI-99*, pages 93–100.
- [Fischer et al., 2014] Fischer, S. C., Blanchard, G. B., Duque, J., Adams, R. J., Arias, A. M., Guest, S. D., and Gorfinkiel, N. (2014). Contractile and Mechanical Properties of Epithelia with Perturbed Actomyosin Dynamics. *PLoS ONE*, 9(4):e95695.
- [Gierer and Meinhardt, 1972] Gierer, A. and Meinhardt, H. (1972). A theory of biological pattern formation. *Kybernetik*, 12(1):30–39.
- [Hutson et al., 2009] Hutson, M. S., Veldhuis, J., Ma, X., Lynch, H. E., Cranston, P. G., and Brodland, G. W. (2009). Combining Laser Microsurgery and Finite Element Modeling to Assess Cell-Level Epithelial Mechanics. *Biophysical Journal*, 97(12):3075–3085.
- [Liu, 2014] Liu, T. (2014). A constitutive model for cytoskeletal contractility of smooth muscle cells. *Proceedings of the Royal Society A: Mathematical, Physical and Engineering Sciences*, 470(2164):20130771–20130771.
- [Lo et al., 2018] Lo, W.-C., Madrak, C., Kiehart, D. P., and Edwards, G. S. (2018). Unified biophysical mechanism for cell-shape oscillations and cell ingression. *Phys. Rev. E*, 97:062414.
- [Madzvamuse and Zenas George, 2013] Madzvamuse, A. and Zenas George, U. (2013). The moving grid finite element method applied to cell movement and deformation. *Finite Elements in Analysis and Design*, 74(0):76–92.

- [Meinhardt, 2006] Meinhardt, H. (2006). From observations to paradigms; the importance of theories and models. an interview with hans meinhardt by richard gordon and lev belousov. *The International journal of developmental biology*, 50(2-3):103–111.
- [Meinhardt, 2008] Meinhardt, H. (2008). Models of biological pattern formation: from elementary steps to the organization of embryonic axes. *Current topics in developmental biology*, 81:1–63.
- [Mercker et al., 2016] Mercker, M., Brinkmann, F., Marciniak-Czochra, A., and Richter, T. (2016). Beyond turing: mechanochemical pattern formation in biological tissues. *Biology Direct*, 11(1):22.
- [Mosca, 2016] Mosca, G. (2016). *Modelling the mechanics of plant morphogenesis*. PhD thesis, University of Bern.
- [Murphy et al., 2016] Murphy, L., Venkataraman, C., and Madzvamuse, A. (2016). A computational approach for mode isolation for reaction-diffusion systems on arbitrary geometries. pages 1–26.
- [Murray, 2002] Murray, J. (2002). *Mathematical Biology I. An Introduction*, volume 17 of *Interdisciplinary Applied Mathematics*. Springer, New York, 3 edition.
- [Murray, 2003] Murray, J. (2003). *Mathematical Biology II: Spatial Models and Biomedical Applications*, volume 18 of *Interdisciplinary Applied Mathematics*. Springer New York.
- [Noll et al., 2017] Noll, N., Mani, M., Heemskerk, I., Streichan, S. J., and Shraiman, B. I. (2017). Active tension network model suggests an exotic mechanical state realized in epithelial tissues. *Nature Physics*, 13(August).
- [Pasakarnis, 2016] Pasakarnis, L. (2016). *Analysis of Acto-myosin Network Remodelling - Towards a Comprehensive Understanding of Tissue Closure Events*. PhD thesis, University of Zurich.
- [Pasakarnis et al., 2016] Pasakarnis, L., Frei, E., Caussinus, E., Affolter, M., and Brunner, D. (2016). Amnioserosa cell constriction but not epidermal actin cable tension autonomously drives dorsal closure. *Nature Cell Biology*, 18(11):1161–1172.
- [Penders et al., 2008] Penders, B., Horstman, K., and Vos, R. (2008). Walking the line between lab and computation: The moist zone. *AIBS Bulletin*, 58(8):747–755.

- [Persson and Strang, 2004] Persson, P.-O. and Strang, G. (2004). A Simple Mesh Generator in MATLAB. *SIAM Review*, 46(2):329–345.
- [Rodriguez et al., 1994] Rodriguez, E. K., Hoger, A., and McCulloch, A. D. (1994). Stress-dependent finite growth in soft elastic tissues. *Journal of Biomechanics*, 27(4):455–467.
- [Ruiz-Baier, 2015] Ruiz-Baier, R. (2015). Primal-mixed formulations for reaction–diffusion systems on deforming domains. *Journal of Computational Physics*, 299:320–338.
- [Ruiz-Baier et al., 2014] Ruiz-Baier, R., Gizzi, A., Rossi, S., Cherubini, C., Laadhari, A., Filippi, S., and Quarteroni, A. (2014). Mathematical modelling of active contraction in isolated cardiomyocytes. *Mathematical Medicine and Biology*, 31(3):259–283.
- [Solon et al., 2009] Solon, J., Kaya-Copur, A., Colombelli, J., and Brunner, D. (2009). Pulsed forces timed by a ratchet-like mechanism drive directed tissue movement during dorsal closure. *Cell*, 137(7):1331–42.
- [Tracqui et al., 2008] Tracqui, P., Ohayon, J., and Boudou, T. (2008). Theoretical analysis of the adaptive contractile behaviour of a single cardiomyocyte cultured on elastic substrates with varying stiffness. *Journal of Theoretical Biology*, 255(1):92–105.
- [Turing, 1952] Turing, A. (1952). The chemical basis of morphogenesis. *Philosophical Transactions of the Royal Society B*, 237:37–72.
- [Volpert and Petrovskii, 2009] Volpert, V. and Petrovskii, S. (2009). Reaction–diffusion waves in biology. *Physics of life reviews*, 6(4):267–310.
- [Wang et al., 2012] Wang, Q., Feng, J. J., and Pismen, L. M. (2012). A Cell-Level Biomechanical Model of Drosophila Dorsal Closure. *Biophysical Journal*, 103(11):2265–2274.
- [Zhivomirov, 2016] Zhivomirov, H. (2016). Phase difference measurement with matlab implementation. URL: <https://ch.mathworks.com/matlabcentral/fileexchange/48025-phase-difference-measurement-with-matlab-implementation>. Accessed 04-08-2018.

gene name	product https://www.pombase.org/	GO cellular component https://www.pombase.org/	Fusion protein localisation								
			GFP(S65T)			mCherry			mGFP		
			EG	DED 0.5h/2h	SD6	EG	DED 0.5h/2h	SD6	EG	DED 0.5h/2h	SD6
adh1	alcohol dehydrogenase	-	C, N	C, N	C, N	-	-	-	-	-	-
suc22	ribonucleotide reductase small subunit	cytosol, nucleus, ribonucleoside- diphosphate reductase complex	N	N	N	-	-	-	-	-	-
pre6	20S proteasome complex subunit alpha 4	cytosol, nuclear periphery, proteasome core complex	-	-	-	-	-	-	C, N	C, N	C, N
dis2	serine/threonine protein phosphatase PP1	cytosol, nucleus, cell tip, nuclear chromatin, cell division site, DPS complex	C, N	C, N	C, N	-	-	-	-	-	-
gln1	glutamate-ammonia ligase	cytosol, nucleus	-	-	-	C, N	C, N	-	-	-	-
tif221	translation initiation factor eIF2B alpha subunit	cytosol, eukaryotic translation initiation factor 2B complex	C	A	C	C	C	C	C	C	C
hsp104	heat shock protein	cytosol, nucleus, nuclear envelope	A	A	N	C, N	C, N	N	C, N	C, N	N
cts1	CTP synthase	cytosol	A	A	-	C, N	C, N	-	C, N	C, N	-

C = cytosolic, N = nuclear, A = assemblies present